CFD BASED AERODYNAMIC MODELING TO STUDY FLIGHT DYNAMICS OF A FLAPPING WING MICRO AIR VEHICLE

by

ALOK ASHOK REGE

Presented to the Faculty of the Graduate School of
The University of Texas at Arlington in Partial Fulfillment
of the Requirements
for the Degree of

MASTER OF SCIENCE IN AEROSPACE ENGINEERING

THE UNIVERSITY OF TEXAS AT ARLINGTON

May 2012

To my parents Anagha and Ashok Rege.

ACKNOWLEDGEMENTS

I express my deep gratitude to my thesis supervisor and mentor Dr. Kamesh Subbarao for putting a lot of faith in me and making me feel that I always belonged here. If only I could achieve half the amount of work he does in a day I would be happy. Doing research and coursework with him has taught me a lot, especially approaching a problem and coming up with new ideas.

It is one of many ideas germinating in his mind that gave me an opportunity to work with Dr. Brian Dennis, whom I cannot thank enough for coming on board as my thesis co-supervisor on such a short notice and allocating his precious time for my research. This work would not have been possible without his exceptional guidance and effort.

I am deeply honored and previleged to have two stalwarts of the Mechanical and Aerospace Department, Dr. Donald Wilson and Dr. Bo Wang in my committee. I thank Dr. Wilson for asking me in my very first graduate advising appointment to meet Dr. Subbarao. I also thank Dr. Wang for teaching me three courses and for showing an earnest interest in my research. I am also thankful to the wonderful MAE staff for their invaluable support and help.

I would like to thank a coterie of brightest minds, my Aerospace Systems Laboratory (ASL) colleagues, for accepting me the way I am and being there for me in many 'Alok' moments. I am also grateful to my CFDLab colleagues for their tremendous help in my research. I would also like to thank all my close friends at UTA for taking the responsibility of being my local guardians.

Finally, I am thankful to my group back home for sticking with me through thick and thin and all my family members for helping me out in every possible way. I would also like to thank my well-wishers for their love and support. I am also grateful to all my past and present teachers who have a played a stellar role in shaping up my career.

Above all, I would like to express my deepest gratitude to my parents Ashok Rege and Anagha Rege, to whom I owe my existence. They cherished my highs, pulled me out of the lows, but most importantly, they made me a good human being.

April 19, 2012

ABSTRACT

CFD BASED AERODYNAMIC MODELING TO STUDY FLIGHT DYNAMICS OF A FLAPPING WING MICRO AIR VEHICLE

ALOK ASHOK REGE, M.S.

The University of Texas at Arlington, 2012

Supervising Professors: Kamesh Subbarao and Brian H Dennis

The demand for small unmanned air vehicles, commonly termed micro air vehicles or MAV's, is rapidly increasing. Driven by applications ranging from civil search-and-rescue missions to military surveillance missions, there is a rising level of interest and investment in better vehicle designs, and miniaturized components are enabling many rapid advances. The need to better understand fundamental aspects of flight for small vehicles has spawned a surge in high quality research in the area of micro air vehicles. These aircraft have a set of constraints which are, in many ways, considerably different from that of traditional aircraft and are often best addressed by a multidisciplinary approach. Fast-response non-linear controls, nano-structures, integrated propulsion and lift mechanisms, highly flexible structures, and low Reynolds aerodynamics are just a few of the important considerations which may be combined in the execution of MAV research.

The main objective of this thesis is to derive a consistent nonlinear dynamic model to study the flight dynamics of micro air vehicles with a reasonably accurate

representation of aerodynamic forces and moments. The research is divided into two sections. In the first section, derivation of the nonlinear dynamics of flapping wing micro air vehicles is presented. The flapping wing micro air vehicle (MAV) used in this research is modeled as a system of three rigid bodies: a body and two wings. The design is based on an insect called Drosophila Melanogaster, commonly known as fruit-fly. The mass and inertial effects of the wing on the body are neglected for the present work. The nonlinear dynamics is simulated with the aerodynamic data published in the open literature. The flapping frequency is used as the control input. Simulations are run for different cases of wing positions and the chosen parameters are studied for boundedness. Results show a qualitative inconsistency in boundedness for some cases, and demand a better aerodynamic data.

The second part of research involves preliminary work required to generate new aerodynamic data for the nonlinear model. First, a computational mesh is created over a 2-D wing section of the MAV model. A finite volume based computational flow solver is used to test different flapping trajectories of the wing section. Finally, a parametric study of the results obtained from the tests is performed.

TABLE OF CONTENTS

ACKNOWLEDGEMENTS iv

ABSTRACT vi

LIST OF ILLUSTRATIONS x

LIST OF TABLES xiv

Chapter Page

1. INTRODUCTION 1

1.1 Flapping Flight:Where it all began 1

1.2 Insect Flapping Flight 3

1.3 Micro Air Vehicles 5

1.4 Literature Review & Thesis Outline 7

2. INSECT MODEL 10

2.1 Examples of Insect Based Models 10

2.2 Flapping Wing MAV Model 11

3. FRAMES OF REFERENCE 14

3.1 Definition 14

3.2 Insect Model Reference Frames 15

3.2.1 Orientation 16

3.2.2 Rotation Matrices 17

4. DERIVATION OF THE EQUATIONS OF MOTION 20

4.1 Governing Physical Principles 20

4.2 Wing and Body Velocities 21

4.3 Aerodynamic Forces and Moments 22

4.4 Governing Equations of Motion 24
5. OPEN LOOP SIMULATION 26
5.1 Simulation Inputs 26
5.2 Open Loop Simulation Studies 27
5.2.1 Discussion on the choice of Dynamic Model Solver 27
5.3 Simulation Results 29
5.4 Remarks 32
6. CFD ANALYSIS 51
6.1 Need for New Aerodynamic Parameters 51
6.2 Computational Fluid Dynamics Approach 52
6.2.1 Computational Grid 53
6.2.2 Flapping Trajectories 56
6.2.3 Computational Flow Solver 58
6.2.4 Data Post-processing 61
7. CFD PARAMETRIC STUDY 62
7.1 C_L-C_D Data Study 62
7.2 Contour Plot Study 64
8. CONCLUDING REMARKS 74
8.1 Summary 74
8.2 Future Work 75
8.2.1 Nonlinear Dynamics with multi-body constraints 75
8.2.2 Determination of Variables for New Aerodynamic Model . . . 75
REFERENCES 77
BIOGRAPHICAL STATEMENT 82

LIST OF ILLUSTRATIONS

Figure Page

1.1 Ancient flapping flight description examples of fig (a) Garuda, a mythical carrier of Lord Vishnu mentioned in Hindu mythology (Image Courtesy:scriptures.ru) and fig (b) Greek mythological character Icarus' attempt to fly using wings made of feathers and wax (Image Courtesy:motls.blogspot.com) 1

1.2 Leonardo Da Vinci's Ornithopter design (Image Courtesy: Anderson, Introduction to flight) 2

1.3 Examples of (a) Bird Stork (Image Courtesy:www.oiseaux-birds.com) and (b) Insect Honey bee (Image Courtesy:utexas. edu) in flight 3

1.4 Insect wing motion (left wing). The black lines denote the instantaneous position of the wing cross-section. The solid circle denotes the wing leading edge 4

1.5 Different types of micro air vehicles (a) Fixed Wing MAV (Image Courtesy: mpower.co.uk), (b) Rotary Wing MAV (Image Courtesy: pixhawk.ethz.ch) and (c) Flapping Wing MAV (Image Courtesy: lr.tudelft.nl) 6

2.1 Examples of insect models used in research, (a) Biomimetic Vehicle used by Oppenheimer et al. [1] for their research and (b) Delfly II (Image Courtesy:TU Delft) 10

2.2 Parts of the flapping wing MAV Model (a) Main Body and (b) Wing 11

2.3 Insect Model (a) Top View of Drosophila Melanogaster and MAV Model (Insect Image Courtesy:jeb.biologists.org) (b) Side View of Drosophila Melanogaster and MAV Model (Insect Image Courtesy:Brown University) 12

3.1 Different Frames of Reference for (a) Aircraft and (b) Insect model 14

3.2 Model Representation with Reference Frames (a) Body frame (b) Right stroke plane and wing frames 15

3.3 Different angles of MAV, (a) Right stroke plane yaw angle χ_R, (b) Pitch angle θ and right stroke plane angle θ_{S_R}, (c) Deviation angles β_R and β_L, (d) Flapping angles ζ_R and ζ_L 17

4.1 Calculation of wing chord $c(r)$ 22

4.2 Wing sectional forces 22

5.1 Case 1 inertial positions and velocities 33

5.2 Case 1 body velocities, angle of attack, sideslip angle and inertial x-z position 33

5.3 Case 1 aerodynamic forces and moments 34

5.4 Case 1 Euler angles and angular rates 34

5.5 Case 1 cycle averaged forces and moments 35

5.6 Case 1 cycle averaged positions 35

5.7 Case 2 inertial positions and velocities 36

5.8 Case 2 body velocities, angle of attack, sideslip angle and inertial x-z position 36

5.9 Case 2 aerodynamic forces and moments 37

5.10 Case 2 Euler angles and angular rates 37

5.11 Case 2 cycle averaged forces and moments 38

5.12 Case 2 cycle averaged positions 38

5.13 Case 3 inertial positions and velocities 39

5.14 Case 3 body velocities, angle of attack, sideslip angle and inertial x-z position 39

5.15 Case 3 aerodynamic forces and moments 40

5.16 Case 3 Euler angles and angular rates 40

5.17 Case 3 cycle averaged forces and moments 41

5.18 Case 3 cycle averaged positions 41

5.19 Case 4 inertial positions and velocities 42

5.20 Case 4 body velocities, angle of attack, sideslip angle and

inertial x-z position 42

5.21 Case 4 aerodynamic forces and moments 43

5.22 Case 4 Euler angles and angular rates 43

5.23 Case 4 cycle averaged forces and moments 44

5.24 Case 4 cycle averaged positions 44

5.25 Case 5 inertial positions and velocities 45

5.26 Case 5 body velocities, angle of attack, sideslip angle and inertial x-z position 45

5.27 Case 5 aerodynamic forces and moments 46

5.28 Case 5 Euler angles and angular rates 46

5.29 Case 5 cycle averaged forces and moments 47

5.30 Case 5 cycle averaged positions 47

5.31 Case 6 inertial positions and velocities 48

5.32 Case 6 body velocities, angle of attack, sideslip angle and inertial x-z position 48

5.33 Case 6 aerodynamic forces and moments 49

5.34 Case 6 Euler angles and angular rates 49

5.35 Case 6 cycle averaged forces and moments 50

5.36 Case 6 cycle averaged positions 50

6.1 Flow chart for CFD analysis 52

6.2 Wing sectional model for CFD analysis 53

6.3 Initial computational domain with (a) Smaller grid size and (b) Coarse mesh 54

6.4 New computational domain with (a) Larger grid size and (b) Refined mesh 55

6.5 Elliptical flapping trajectory with (a) Flapping direction and (b) Instantaneous wing positions 57

6.6 Straight flapping trajectory with (a) Flapping direction and

(b) Instantaneous wing flapping positions 57

6.7 Figure-8 flapping trajectory with (a) Flapping direction and (b) Instantaneous wing flapping positions 58

6.8 Optimal flapping trajectory obtained by Ueno et al. [2] with (a) Flapping direction and (b) Instantaneous wing flapping positions 59

6.9 Unstructured mesh around the wing section with smoothing and remeshing employed 60

7.1 Aerodynamic coefficients plot for 51st cycle of elliptical trajectory 66

7.2 C_{Lavg} convergence plot for elliptical trajectory 66

7.3 Aerodynamic coefficients plot for 51st cycle of straight line trajectory 67

7.4 C_{Lavg} convergence plot for straight line trajectory 67

7.5 Aerodynamic coefficients plot for 51st cycle of Figure-8 trajectory 68

7.6 C_{Lavg} plot for Figure-8 trajectory 68

7.7 Aerodynamic coefficients plot for 51st cycle of flapping trajectory from Ueno et al. [2] 69

7.8 C_{Lavg} plot for flapping trajectory from Ueno et al. [2] 69

7.9 Velocity vector plot for elliptical trajectory 70

7.10 Velocity vector plot for straight line trajectory 71

7.11 Velocity vector plot for Figure-8 trajectory 72

7.12 Velocity vector plot for flapping trajectory from Ueno et al. [2] 73

LIST OF TABLES

Table		Page
2.1	Characteristics of Drosophila Melanogaster	12
5.1	Properties of MAV model	26
5.2	Body Inertia Tensors of MAV model	27
5.3	Open Loop Simulation Cases	28
6.1	Smoothing Parameters for Dynamic Mesh of MAV model	60
6.2	Reference Values for calculation of Lift coefficient C_L	61

CHAPTER 1

INTRODUCTION

1.1 Flapping Flight:Where it all began

The history of flapping flight has a long and storied road. For centuries, humans have been fascinated by flapping flight. In Hindu mythology, there is a description of a mythical bird-like creature named Garuda [fig 1.1(a)], known to be a carrier of Lord Vishnu. Humans have also toyed with idea of mimicing the bird flight themselves, like Icarus' vain attempt at flying using wings made of feathers and wax as described in Greek mythology [fig 1.1(b)]. The first writings on trying to use the idea of flapping flight date all the way back to the 4th century BC in the ancient epic Ramayana, but there were not any details of the designs in the descriptions.

(a) (b)

Figure 1.1. Ancient flapping flight description examples of fig (a) Garuda, a mythical carrier of Lord Vishnu mentioned in Hindu mythology (Image Courtesy:scriptures.ru) and fig (b) Greek mythological character Icarus' attempt to fly using wings made of feathers and wax (Image Courtesy:motls.blogspot.com).

Since birds seem to fly with little or no effort, the earliest designs in flapping flight emulated birds. The first person to research the flight of birds in depth was a legend of the Renaissance, Leonardo da Vinci. He began studying the flight of birds in the late 15th century and designed sketches a model known as the Ornithopter [fig 1.2], which in Greek means "bird wing". The sketches of the Ornithopter made by Da Vinci used a system of pulleys and gears powered by the arms and legs that would make the wings move in the fashion that a bird's wing does. Da Vinci's design was not based on an idea of having a wing attached to each arm of a human and having that person flap his arms up and down because he discovered that humans were not strong enough to generate the power needed to fly. Da Vinci did not make a full scale model of his design, but his work set the tone for many other future innovators and engineers to investigate the flapping flight phenomenon in more detail.

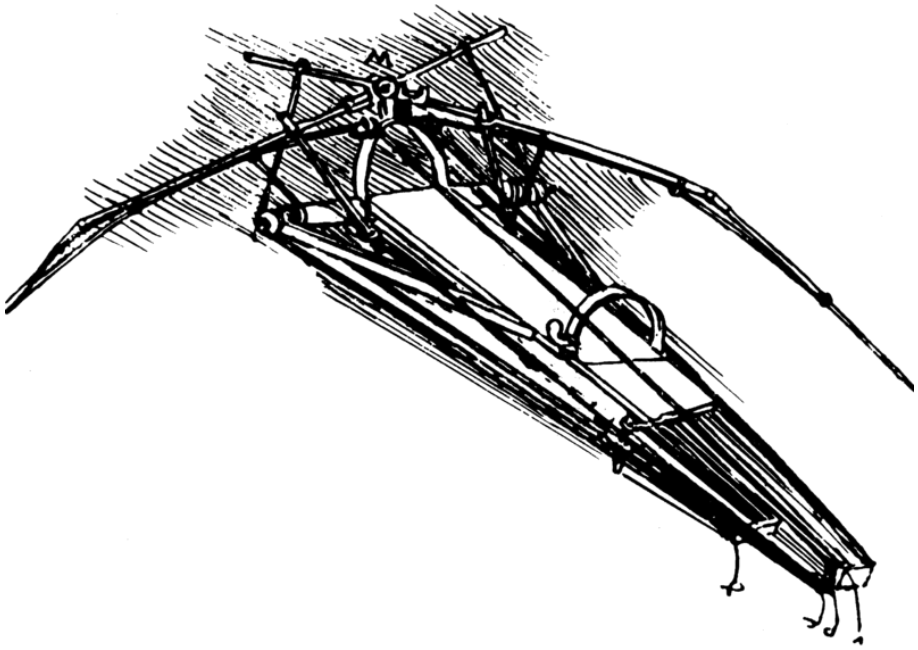

Figure 1.2. Leonardo Da Vinci's Ornithopter design (Image Courtesy:Anderson, Introduction to flight).

1.2 Insect Flapping Flight

The flapping or beating motion of wings is exclusively used in the powered flight of birds and insects to counter the gravity force and propel themselves against aerodynamic drag. The mode and frequency of the flapping motion differ among different species and are strongly dependent on the body size, shape and flight mode. They are however always selected for the optimal power consumption of the respective flight modes. The difference between flapping motion of birds and insects is in the way they use the aerodynamic forces, lift and drag. In birds, the Reynolds number (Re), which is the ratio of inertial forces to viscous forces, and the wing aspect ratio are so large that they deliberately use their wings to sustain their weight by lift. With large wing span and high aspect ratio they they can achieve long-range flight by maximizing C_L/C_D ratio or long-duration flight by maximizing $C_L^{3/2}/C_D$ ratio.

(a) (b)

Figure 1.3. Examples of (a) Bird Stork (Image Courtesy:www.oiseaux-birds.com) and (b) Insect Honey bee (Image Courtesy:utexas.edu) in flight.

In insects, however, the Reynolds number and the aspect ratio are too small to provide the necessary lift. Instead, they use high frequency flapping and different flapping trajectories to get high values of the required C_L/C_D and $C_L^{3/2}/C_D$ ratios.

Infact, insects owe much of their extraordinary evolutionary success to flight. Because their survival and evolution depend so crucially on flight performance, different flight related sensory, physiological, behavorial and biomechanical traits of insects are among the most compelling illustrations of adaptations found in nature.

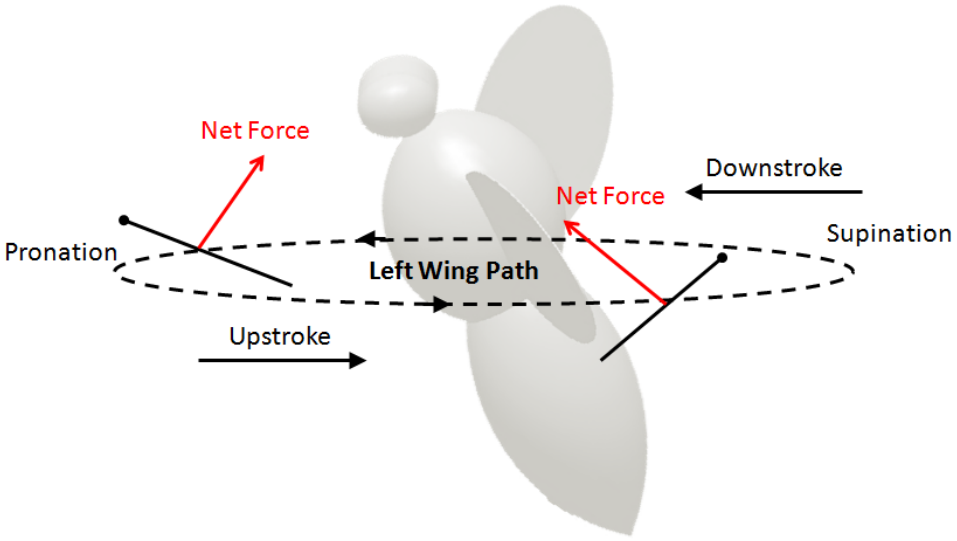

Figure 1.4. Insect wing motion (left wing). The black lines denote the instantaneous position of the wing cross-section. The solid circle denotes the wing leading edge.

The flapping motion of an insect can be decomposed into three separate motions:sweeping or flapping (forward and backward movement of wings), heaving (up and down movement) and pitching (changing incidence angle). In fig 1.4, a schematic representation of left wing motion of an insect is shown. A complete flap cycle for a sophisticated insect wing motion consists of twice a translation (a downstroke and an upstroke) and twice a rotation (termed pronation at the end of the down-stroke and supination at the end of the up-stroke). During the translation the wing may show a sweeping, heaving and pitching motions. In addition, at the end of a half-stroke during stroke reversal (rotation) the wing pitches rapidly. The exact wing kinemat-

ics varies among different insects and for different motions in flight. Insects may change their stroke angle, angle of attack and wing rotation to perform desired flight maneuvers [3].

Insects have generated a great deal of interest among biologists and engineers, because at first glance, their flight seems improbable using standard aerodynamics theory. The combination of small size, high stroke frequency and peculiar reciprocal flapping motion of insects make their flight aerodynamics unintelligible. However, researchers have benefitted greatly from the availability of high-speed video capturing wing kinematics, new methods such as digital particle image velocimetry (DPIV) to quantify flows, and powerful computers for simulation and analysis. It is this more detailed knowledge of kinematics, forces and flows that has led to significant progress in our understanding of insect flight aerodynamics.

1.3 Micro Air Vehicles

Micro Air Vehicles or MAV's, are small unmanned aerial vehicles of size less than fifteen centimeters as defined by DARPA (Defense Advanced Research Projects Agency) in their MAV development program. It must be noted that MAV's are not smaller versions of larger aircraft. They should be seen as aerial robots having more degree of freedom and agility than regular aircraft, which puts them in a class of their own. These flyers have a set of constraints which are, in many ways, considerably different from that of traditional aircraft and are often best addressed by a multidisciplinary approach.

The dream of building MAV's could become a reality due to the recent developments in micro-technologies, be it developing control equipments with the help of micro-electrical-mechanical systems (MEMS), or reducing the order of cameras and sensors that could be fitted on these vehicles. As such, MAV's have wide range of

applications because of their small size and very high maneuverability. They could be used in surveillance of battlefields and urban areas. They could also be used in the detection of biological agents, chemical compounds and nuclear or radioactive materials. A fleet of MAV's could be sent to improve communication in urban or other environments requiring continuous operations. They could also be used to fly in confined spaces, such as collapsed buildings to locate survivors or in fire rescue or counter-drug operations.

MAV's can be classified into three types: fixed wing, rotary wing or flapping wing as shown in fig 1.5.

(a) (b) (c)

Figure 1.5. Different types of micro air vehicles (a) Fixed Wing MAV (Image Courtesy: mpower.co.uk), (b) Rotary Wing MAV (Image Courtesy: pixhawk.ethz.ch) and (c) Flapping Wing MAV (Image Courtesy: lr.tudelft.nl).

Flapping wing MAV's are bio-inspired, i.e., they try to mimic insect flight. Designs of such MAV's, if realized, could achieve unprecedented flight capabilites of an insect. This has sparked off a surge in high quality research in the area of flapping wing MAV research.

1.4 Literature Review & Thesis Outline

Preliminary work into the flight dynamics of flapping wing MAV's is taken from the analysis of the flight mechanics and stability of specific insects. Weis-fogh [4] produced a seminal paper on the analytical expressions to estimate the forces on the wings of various insects and the work and power produced. Ellington in [5, 6, 7, 8, 9, 10] provided a complete overview of the insect flight, right from kinematics to lift and power requirements for hovering. Zanker in [11, 12] gave an insight into the flight dynamics of Drosophila Melanogaster. Taylor et. al [13] used the linearized equations of rigid body motion, available in [14] to study the flight stability of the desert locust Schistocerca gregaria. The mass of the wings, and the associated gyroscopic terms, were neglected due to the assumption that the wings beat fast enough to not excite the rigid body modes of the central body. In [15], Sun et. al used the same rigid body approximation as in [13] to analyze the hovering flight stability of a bumblebee. The stability derivatives were obtained from computational fluid dynamics using flight data from [16]. Doman et. al in [17, 18] presented modeling and control of a flapping wing MAV based on the RoboFly developed by Wood and presented in [19]. The aerodynamic model used in the simulations was developed in [17] and based on the work of Sane et. al [20]. The cycle-averaged aerodynamic forces and moments were presented in detail, along with calculation of the control derivatives based on the dynamic and aerodynamic models.

Sun et. al presented a derivation of the equations of motion for an insect in [21]. The wings were modeled with three degrees of freedom. The motion of the wings was prescribed and the wings were not considered to be separate degrees of freedom. The equations of motion were derived using Eulerian techniques. In [22], Wu et. al presented simulations of the equations of motion, previously derived by Sun et al. in [21]. The authors presented a method of solving the required parameters for a

hover condition by coupling the equations of motion with the Navier-Stokes equations. In [23], Gebert et al. derived the equations of motion for a flapping wing MAV using Newtonian methods, which required the calculation of the constraint forces between the wings and the body. The wings were not neglected, but simulations were not presented to validate the efforts. Furthermore, Sun et al. claim in [21] that the equations of motion derived in [23] contain errors and cannot be used. Orlowski et. al in [24] provided the modeling and simulation of nonlinear dynamic model using a quasi-static approach. The simulations results were shown for three cycles of flap.

Many researchers have worked on understanding and presenting the aerodynamics surrounding the insect flight. In [25], Shyy et. al offered an overview of the challenges and issues involved in using computational modeling of aerodynamic forces. In [26], Sun et. al studied the lift and power requirements of hovering insect flight by solving the Navier-Stokes equations numerically. Jane Wang in [27] proved using computational methods that a two dimensional hovering motion can generate enough lift to support a typical insect weight. Ramamurti in [28] verified the hypothesis presented by Dickinson et. al in their germinal work on mechanical Drosophila wings in [29] that rotational mechanisms of the wing form the basis by which the insect modulates the magnitude and direction of forces during flight. They employed a finite element flow solver to compute an unsteady flow past a 3-D Drospophila wing undergoing flapping motion. Bai et. al in [30] proposed a new bionic flapping motion for Drosophila wing using CFD techniques. They justified the correctness of their numerical method and the computational program by comparing their CFD results of the Drosophila flapping motion in three modes, i.e., the advanced mode, the symmetrical mode and the delayed mode, with Dickinson's experimental results from [29].

The thesis work presented deals with the modeling and simulation of a nonlinear dynamic model which could be scalable, in the sense of accomodating aerodynamic and flight features of different insects. A CFD approach is followed to do the preliminary work for developing a new aerodynamic model. The insect model used for this research is described in Chapter 2. Chapter 3 talks about the different reference frames involved in the derivation of the nonlinear dynamics, which is presented in Chapter 4. Chapter 5 presents the open loop simulation results for various parameters. Chapter 6 gives an overview of the CFD analysis performed for different flapping trajectories of a 2-D wing section of the flapping wing MAV. Chapter 7 discusses the results of the CFD parametric study, while concluding remarks are presented in Chapter 8.

CHAPTER 2

INSECT MODEL

2.1 Examples of Insect Based Models

Various researchers have been using different insects for their bio-inspired flight study. Both Weis-Fogh [4] and Ennos [31] worked extensively on different diptera insects. While in [32] Azuma et al. studied the flight mechanics of a Dragonfly, Tobalske et al. in [33] focussed their research on the hummingbird flight. Sun [34, 35], Bai [30] and Zanker [11] chose Drosophila Melanogaster for their research.

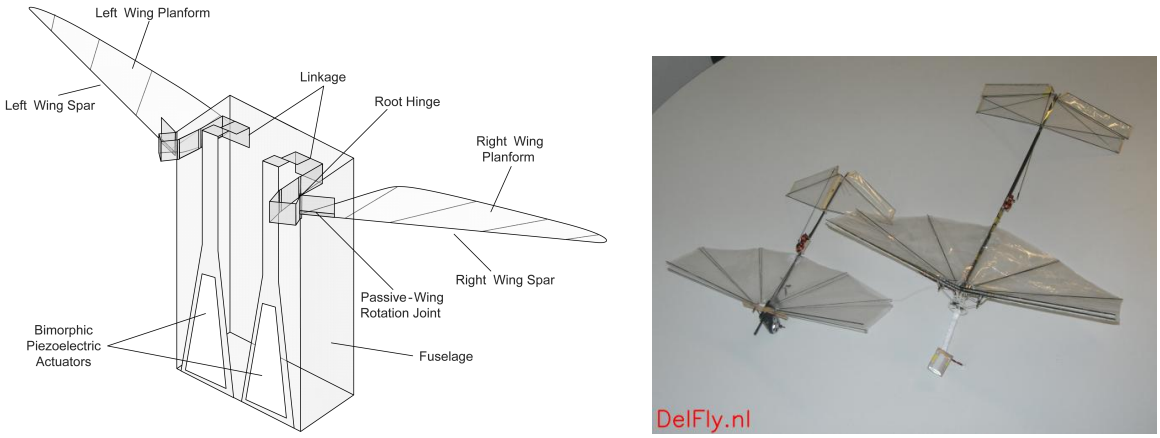

(a) (b)

Figure 2.1. Examples of insect models used in research, (a) Biomimetic Vehicle used by Oppenheimer et al. [1] for their research and (b) Delfly II (Image Courtesy:TU Delft).

Researchers have also worked on models based on insects for their flapping flight study. Orlowski [24] used a simplistic flapping wing MAV model with a cylinder as a central body and two rectangular thin flat plates as wings. Dickinson [29] used a

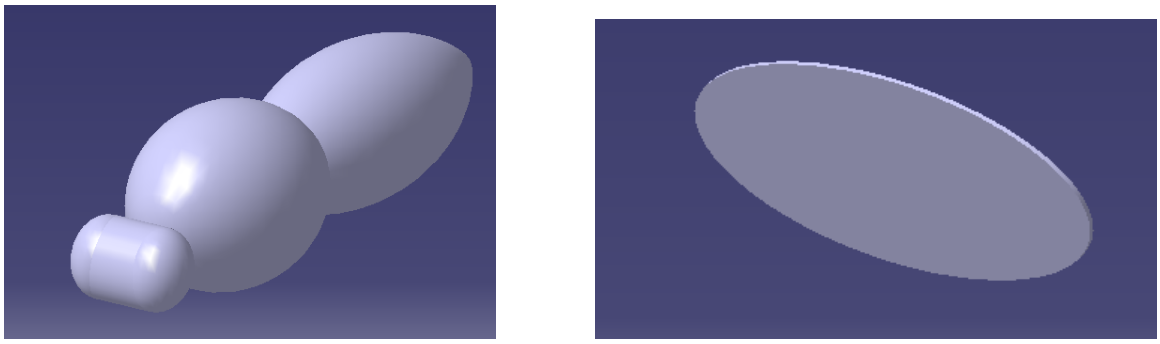

(a) (b)

Figure 2.2. Parts of the flapping wing MAV Model (a) Main Body and (b) Wing.

dynamically scaled model of Drosophila Melanogaster for the experimental research. Oppenheimer et al. [1] worked on the dynamics and control of a minimally actuated flapping wing MAV shown in fig 2.1(a). Groen [36] did an aerodyanmic and aeroelastic investigation of vortex development on Delfly II shown in fig 2.1(b), which was built by the research team of TU Delft. Liu in [37] addressed an integrated and rigorous model for the simulation of an insect flapping flight.

2.2 Flapping Wing MAV Model

The model of the flapping wing MAV is based on Drosophila Melanogaster, commonly known as fruit-fly. Typical characteristics of Drosophila were obtained from Azuma [38] and are tabulated in Table 2.1.

The MAV model was designed using the design software CATIA V5. The model was conceptualized having three rigid bodies; a main body with two wings symmetrically attached to it. As shown in fig 2.2(a), the main body is made up of three ellipsoidal shapes depicting the head,thorax and abdomen of the insect. The wings are modeled as thin, flat elliptical plates with variable chord as shown in fig 2.2(b). The values of mass and inertia tensors of each body were calculated separately using the measurements tool in CATIA.

Table 2.1. Characteristics of Drosophila Melanogaster

Property	Value
Reynolds Number, Re	75<Re<225
Mass, m	2 mg
# of Wings	2
Wing semi-span, b	3 mm
Wing Flapping Frequency, f	240 Hz
Stroke Amplitude	160 deg

The three parts were then assembled using the assembly toolbox in CATIA. The constraints were set in such a way that would enable the wings to have 3 degrees

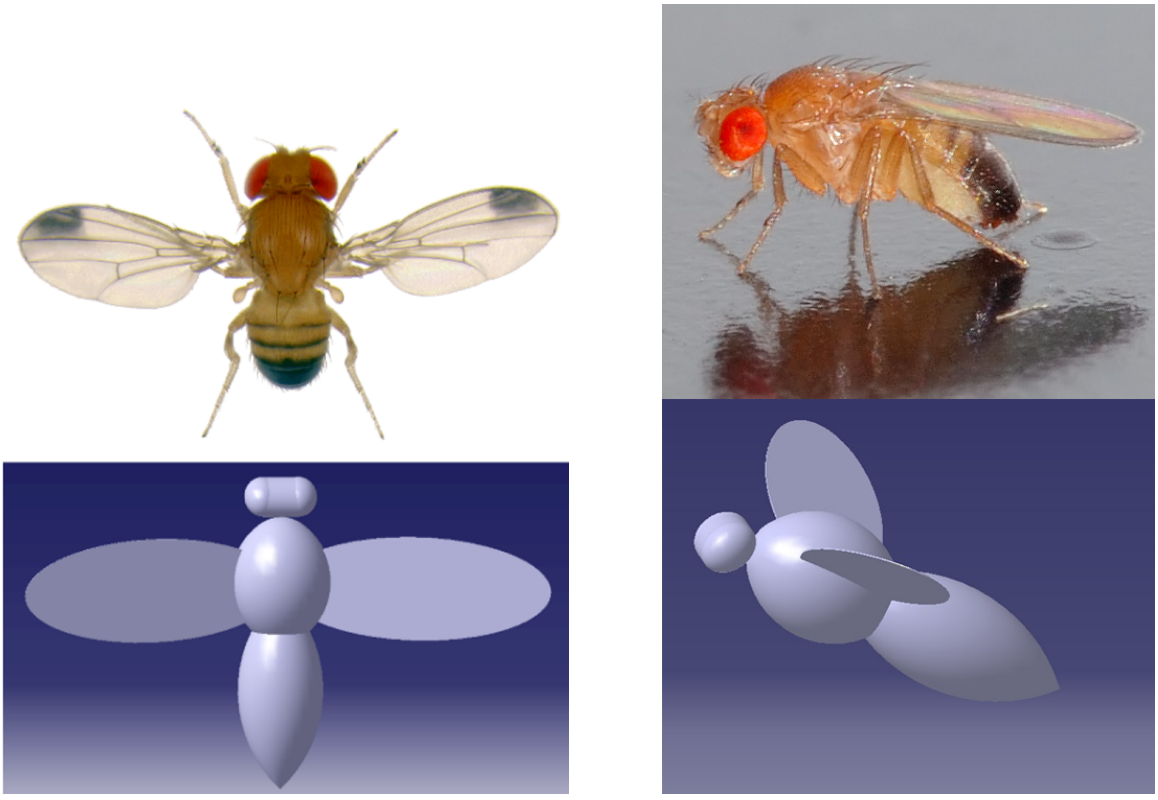

(a) (b)

Figure 2.3. Insect Model (a) Top View of Drosophila Melanogaster and MAV Model (Insect Image Courtesy:jeb.biologists.org) (b) Side View of Drosophila Melanogaster and MAV Model(Insect Image Courtesy:Brown University).

of freedom motion. Given the DMU Kinematics toolbox in CATIA V5, one could also visualize the 3-DOF flapping motion of the wings. Fig 2.3 shows the insect and the model in top view [fig 2.3(a)] and in side view [fig 2.3(b)].

Although the flapping wing MAV model is based on fruit fly, it can be used to simulate the motions of different insects using appropriate characteristics and parameters of the specific insect.

CHAPTER 3

FRAMES OF REFERENCE

3.1 Definition

Frame of reference is a set of coordinate axes with reference to which the position or motion of an object is described or physical laws are formulated. Defining frames of reference is of prime importance in flight dynamics, for the forces realized with respect to one reference frame may be different than that with respect to another. As shown in fig 3.1(a), a typical aircraft has three reference frames. Inertial reference frame is the earth fixed frame. A rotation matrix T_I^B is used to go from the inertial reference frame to the Body frame, which is fixed at the center of mass of the aircraft. Similarly a rotation matrix T_B^W is used to go to the Wind frame.

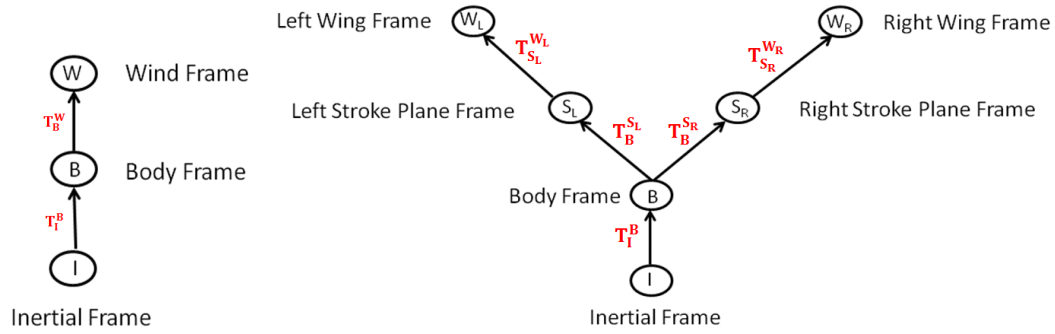

Figure 3.1. Different Frames of Reference for (a) Aircraft and (b) Insect model.

3.2 Insect Model Reference Frames

To accurately describe the motion of the body with respect to an inertial frame, and the motion of the wings with respect to the body, six reference frames are specified as shown in fig 3.1(b). The first reference frame is an inertial frame. The absolute velocity and position of the FWMAV is described with respect to the Inertial frame. The Body frame is a body-fixed coordinate system attached to the main body of the FWMAV with origin at the center of mass of the body and is depicted in Fig 3.2(a). The frame is oriented with positive x-axis along the longitudinal axis of the central body. The y-axis is perpendicular to the x-axis and is positive out of the right side of the vehicle. The z-axis is positive downward and perpendicular to the x-y plane. An x-z plane of mass symmetry is assumed for the main body.

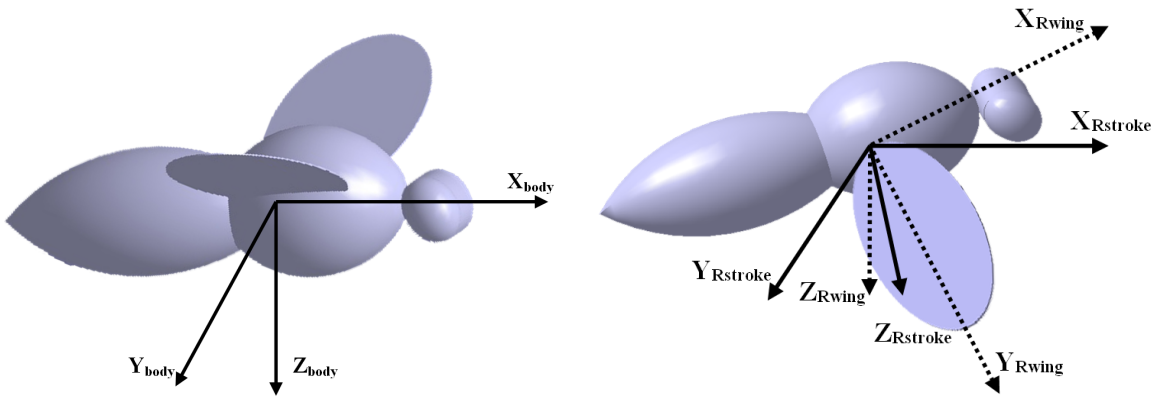

Figure 3.2. Model Representation with Reference Frames (a) Body frame (b) Right stroke plane and wing frames.

In addition to the Body frame, the stroke plane frames are two body-fixed frames originated at the wing joints. The stroke plane frames are denoted by 'S_R' and 'S_L', where 'R' and 'L' stand for right and left respectively. The stroke plane frames have initial orientation parallel to the Body frame. The stroke plane defines the mean

motion of the wing. The attitude of the stroke plane with respect to the Body frame is given by two consecutive rotations about body z-axis and y-axis through stroke plane yaw angle 'χ' and stroke plane angle 'θ_s' respectively. The initial orientation of the wing frames is parallel to the stroke plane frames with an origin coincident with the wing joint. The wing frames, 'W_R' and 'W_L', move with the rotation of the wings and enable the calculation of the wings' orientations with respect to the stroke plane, and by extension, the main body. The right stroke plane and the wing frames are depicted in Fig 3.2(b). The stroke plane frame is represented by solid lines. The wing frame is represented by dotted lines.

3.2.1 Orientation

The orientation of the main body is determined by 3-2-1 Euler angles with respect to the inertial (fixed) frame. The orientation of the stroke plane with respect to the body is denoted by the stroke plane yaw angles 'χ_R' and 'χ_L' and the stroke plane angles θ_{S_R} and θ_{S_L} and is fixed for a given flight condition. Fig 3.3(a) shows the stroke plane yaw angle.

The orientation of the wings with respect to the stroke plane is determined by the deviation, pitch and flap angles of the wings β, θ and ζ respectively. The stroke plane angle and the pitch angle are shown in fig 3.3(b). The relation of deviation angle β and flapping angle ζ to the main body are shown in fig 3.3(c) and fig 3.3(d) respectively. Positive rotations are consistent with the right hand rule. A positive pitch angle is up in the stroke plane frame. A positive deviation angle is up and a positive flap angle (sweep) is forward.

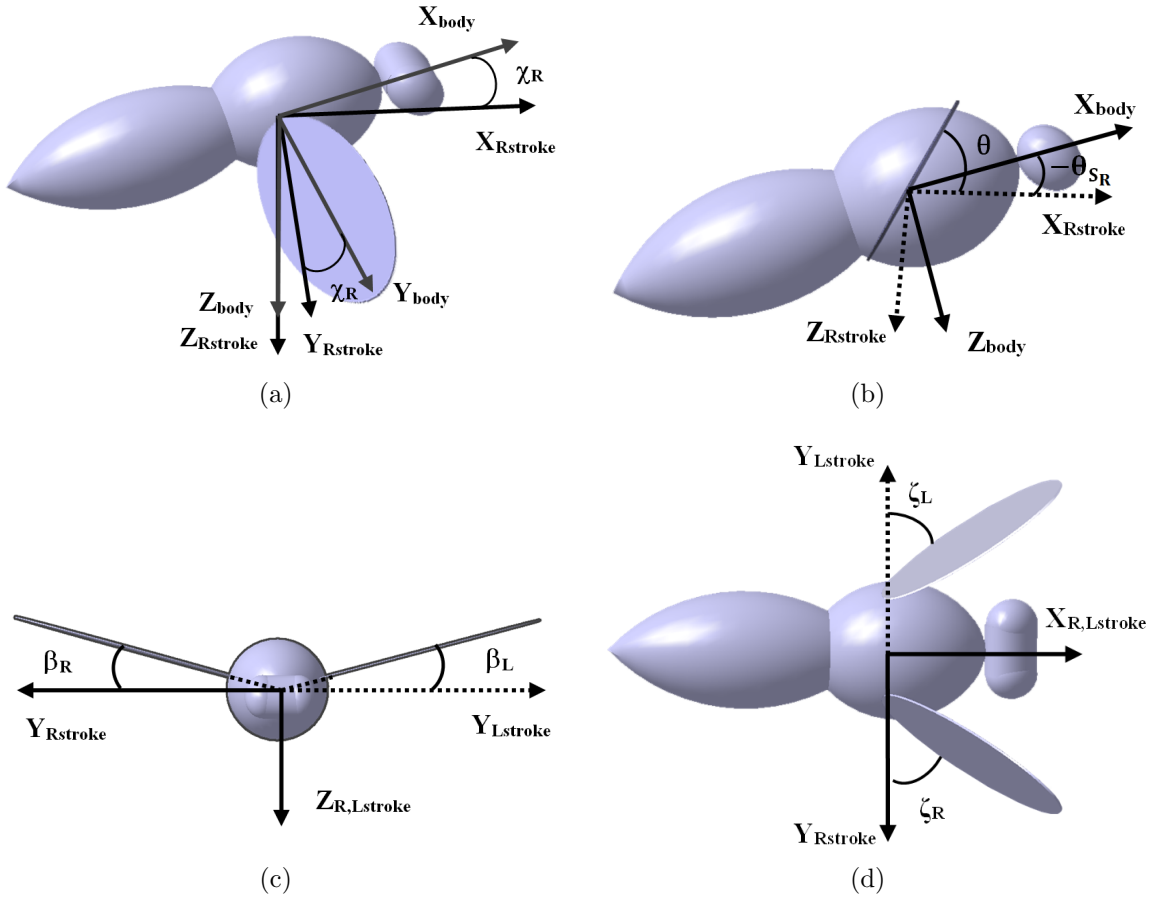

Figure 3.3. Different angles of MAV, (a) Right stroke plane yaw angle χ_R, (b) Pitch angle θ and right stroke plane angle θ_{S_R}, (c) Deviation angles β_R and β_L, (d) Flapping angles ζ_R and ζ_L.

3.2.2 Rotation Matrices

The rotation matrix from the inertial frame to Body frame, T_I^B, is determined by proper combination of the 3-2-1 Euler angles performed by quaternion, $\vec{Q} = q_0 + q_1\hat{i} + q_2\hat{j} + q_3\hat{k}$, to avoid any singularities. The rotation matrix using quaternion formulation is given by

$$T_I^B = \begin{bmatrix} q_0^2 + q_1^2 - q_2^2 - q_3^2 & 2(q_1q_2 + q_0q_3) & 2(q_1q_3 - q_0q_2) \\ 2(q_2q_1 - q_0q_3) & q_0^2 - q_1^2 + q_2^2 - q_3^2 & 2(q_2q_3 + q_0q_1) \\ 2(q_3q_1 + q_0q_2) & 2(q_3q_2 - q_0q_1) & q_0^2 - q_1^2 - q_2^2 + q_3^2 \end{bmatrix} \tag{3.1}$$

The rotation matrices for the stroke plane are

$$T_{\chi} = \begin{bmatrix} \cos\chi & -\sin\chi & 0 \\ \sin\chi & \cos\chi & 0 \\ 0 & 0 & 1 \end{bmatrix},$$
$$T_{\theta_S} = \begin{bmatrix} \cos\theta_S & 0 & -\sin\theta_S \\ 0 & 1 & 0 \\ \sin\theta_S & 0 & \cos\theta_S \end{bmatrix}, \tag{3.2}$$

The rotation matrices are combined according to

$$T_B^{S_{R,L}} = T_{\theta_{S_{R,L}}} T_{\chi_{R,L}} \tag{3.3}$$

where subscripts R and L are attached to denote the proper stroke plane frame. The orientation for the right and left wings with respect to the S_R and S_L frames is determined by the 3-1-2 Euler angles, where $\zeta = 3$, $\theta = 2$, $\beta = 1$. The singularity for this sequence is at the deviation angle $\beta = \pm 90°$, which will never be achieved by the wing stroke kinematics. So the 3-1-2 Euler angles physically satisfy the requirements of the system. The rotation matrices for the right wing are

$$T_{\beta_R} = \begin{bmatrix} 1 & 0 & 0 \\ 0 & \cos\beta_R & -\sin\beta_R \\ 0 & \sin\beta_R & \cos\beta_R \end{bmatrix},$$
$$T_{\theta_R} = \begin{bmatrix} \cos\theta_R & 0 & -\sin\theta_R \\ 0 & 1 & 0 \\ \sin\theta_R & 0 & \cos\theta_R \end{bmatrix}, \tag{3.4}$$
$$T_{\zeta_R} = \begin{bmatrix} \cos\zeta_R & -\sin\zeta_R & 0 \\ \sin\zeta_R & \cos\zeta_R & 0 \\ 0 & 0 & 1 \end{bmatrix}$$

The rotation matrices are combined according to

$$T_{S_R}^{W_R} = T_{\theta_R} T_{\beta_R} T_{\zeta_R} \tag{3.5}$$

The rotation matrices for the left wing, with respect to the left stroke plane, are combined in the same manner as in eq (3.4). The negative signs for the rotation matrices for the ζ and β angles are interchanged for the right and left wings. This is due to the fact that flapping motion is considered positive when the wings move forward, which is a positive rotation for the left wing by the angle ζ_L, but a negative rotation for the right wing by the angle ζ_R. Similarly, positive upward deviation is a negative rotation of the angle β_R for the right wing, but a positive rotation by the angle β_L for the left wing. The correct sign ensures proper cancellation of forces and moments in the Body frame when the flapping is symmetrical, which will be discussed later.

CHAPTER 4

DERIVATION OF THE EQUATIONS OF MOTION

4.1 Governing Physical Principles

In this section, the development of a nonlinear dynamic model of FWMAV derived from first principles is described. The derivation of a set of nonlinear, 6-DOF equations of motion of FWMAV is similar to that adopted for a standard aircraft model stated in [14]. Here the aerodynamic forces and moments generated due to the flapping of wings are equated to the rate of change of linear momentum and angular momentum respectively to form the set of equations.

Newton's Law of Linear Motion:

$$\frac{d}{dt}\left[\int_V \rho_A \frac{dr'}{dt} dV\right] = \int_V g\rho_A dV + \int_S F ds \tag{4.1}$$

Euler's Law of Angular Motion:

$$\frac{d}{dt}\left[\int_V r' \times \rho_A \frac{dr'}{dt} dV\right] = \int_V r' \times g\rho_A dV + \int_s r' \times F ds \tag{4.2}$$

In eq (4.1), the L.H.S. denotes the rate of change of linear momentum of the FWMAV which is equated to the applied forces (Gravitational + Aerodynamic). Similarly in eq (4.2), the L.H.S. denotes the rate of change of angular momentum which is equated to the applied moments. In eqs (4.1) and (4.2), is the position vector of a small elemental mass of volume dV and density ρ_A. g is the acceleration due to gravity (assumed constant), Fds represents the elemental surface forces (aerodynamics).

4.2 Wing and Body Velocities

The velocities of each of the bodies will be defined for forces and moments calculation. The angular velocities of the wings are a function of the wing angles and angular rates. The angular velocities of the wings, with respect to the stroke plane, are calculated according to the 3-1-2 Euler angle relationship. The angular velocity of the right wing with respect to the right stroke plane is calculated according to

$$\vec{\omega}_{Rwing} = T_{\theta_R} T_{\beta_R} \begin{bmatrix} 0 \\ 0 \\ -\dot{\zeta}_R \end{bmatrix} + T_{\theta_R} \begin{bmatrix} -\dot{\beta}_R \\ 0 \\ 0 \end{bmatrix} + \begin{bmatrix} 0 \\ \dot{\theta}_R \\ 0 \end{bmatrix} \tag{4.3}$$

The velocity of the right wing root in body frame with respect to inertial frame is given by

$$\vec{V}_{Rwing} = \vec{U} + \left(\vec{\Omega} \times \vec{R}_R \right) \tag{4.4}$$

where $\vec{R}_R$ is the position of wing root from the main body center of mass; $\vec{U}$ is the linear velocity of the FWMAV and in the body frame components is given by

$$\vec{U} = u\hat{i} + v\hat{j} + w\hat{k} \tag{4.5}$$

and $\vec{\Omega}$ is the angular velocity of the FWMAV and in the body frame components is given by

$$\vec{\Omega} = p\hat{i} + q\hat{j} + r\hat{k} \tag{4.6}$$

In stroke plane frame, the velocity can be written as

$${}_{S_R}V_{Rwing} = T_B^{S_R} \left[U + (\Omega \times R_R) \right] \tag{4.7}$$

The total angular velocity of right wing with respect the right stroke plane frame is

$$\vec{\Omega}_{Rwing} = T_B^{S_R} \vec{\Omega} + \vec{\omega}_{Rwing} \tag{4.8}$$

The total linear velocity of right wing with respect the right stroke plane frame is

$$\vec{U}_{Rwing} = {}_{S_R}V_{Rwing} + \vec{\Omega}_{Rwing} \times \vec{r}_{Rwing} \tag{4.9}$$

where $\vec{r}_{Rwing}$ is the position vector of the wing element from the wing root. A similar procedure is used to develop the velocity expressions for the left wing. It is important to note, consistent with the development of the orientation of the wings with respect to the stroke planes and the right hand rule, that the signs are opposite for $\dot{\beta}_R$ and $\dot{\beta}_L$ and $\dot{\zeta}_R$ and $\dot{\zeta}_L$, which results (for symmetric flapping) in equal and opposite rolling and yawing moments in the Body frame.

4.3 Aerodynamic Forces and Moments

The forces and moments are developed on the body due to the motion of the wing. The method used to calculate these forces and moments has been adopted from Azuma [38]. Fig 4.1 shows the elliptical right wing in the right wing frame with X_{Rwing} and Y_{Rwing} as x-axis and y-axis repectively. Let r_{max} be the total length of the wing, while $chord_{max}$ be the maximum chord length. Consider a small elemental strip dr at a length r_{st} from the wing root.

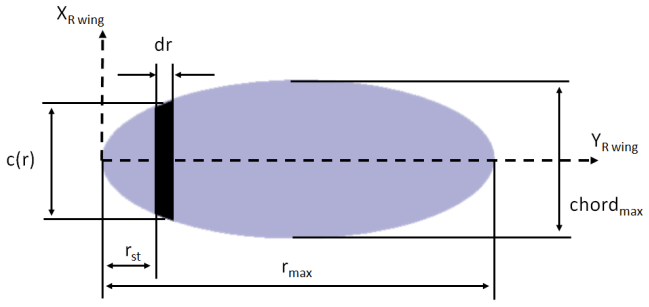

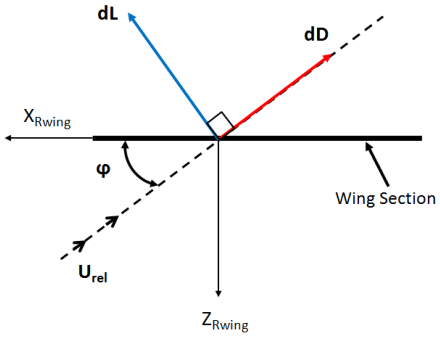

Figure 4.1. Calculation of wing chord $c(r)$. Figure 4.2. Sectional forces on right wing.

Then the corresponding chord length of the wing is given by

$$c(r) = chord_{max}\sqrt{1 - 4\left(\frac{r_{st}}{r_{max}} - \frac{1}{2}\right)^2} \tag{4.10}$$

Now consider a section of the right wing in the X_{Rwing}-Z_{Rwing} plane as shown in fig 4.2. By neglecting the flow along the wing span, the relative velocity of air acting at a right wing element is given by

$$U_{rel} = \sqrt{u_{Rwing}^2 + w_{Rwing}^2} \tag{4.11}$$

where

u_{Rwing} = velocity component in x-direction;

w_{Rwing} = velocity component in z-direction

The inflow angle is given by

$$\varphi_R = \tan^{-1}\left(\frac{w_{Rwing}}{u_{Rwing}}\right) \tag{4.12}$$

The total angle of attack acting on the wing element is given by

$$\alpha_R = \theta_R + \varphi_R \tag{4.13}$$

Equations of lift and drag are given by

$$\begin{aligned} dL_R &= \tfrac{1}{2}\rho U_{rel}^2 C_L(\alpha_R)c(r)dr \\ dD_R &= \tfrac{1}{2}\rho U_{rel}^2 C_D(\alpha_R)c(r)dr \end{aligned} \tag{4.14}$$

The expressions for C_L and C_D calculation are taken from Dickinson et al [20], which are given as

$$\begin{aligned} C_D(\alpha) &= 1.92 - 1.55\cos(2.04\alpha - 9.82) \\ C_L(\,\alpha) &= 0.225 + 1.58\sin(2.13\alpha - 7.2) \end{aligned} \tag{4.15}$$

While the lift and drag coefficients are assumed to be similar to that in [20], the nonlinear dynamical model is quite scalable in the sense that when accurate lift

and drag coefficients are available, they can be easily substituted for the equations above. The forces acting on the right wing element are then given by

$$d\vec{F}_{Rwing} = \begin{bmatrix} dL_R \sin\varphi_R - dD_R \cos\varphi_R \\ 0 \\ -dL_R \cos\varphi_R - dD_R \sin\varphi_R \end{bmatrix} \tag{4.16}$$

The moments acting on the right wing element are given by

$$d\vec{M}_{Rwing} = \vec{r}_{Rwing} \times d\vec{F}_{Rwing} \tag{4.17}$$

The elemental forces and the moments are then integrating along the entire wing length to get the total aerodynamic forces and moments on the right wing. Similar procedure is followed to get forces and moments on the left wing. The forces and moments are then expressed in the body frame.

The total aerodynamic forces in the body frame are given by

$$\vec{F}_{aero} = \left[T_B^{S_R}\right]^T \left[T_{S_R}^{W_R}\right]^T \vec{F}_{Rwing} + \left[T_B^{S_L}\right]^T \left[T_{S_L}^{W_L}\right]^T \vec{F}_{Lwing} \tag{4.18}$$

Similarly, the total aerodynamic moments in the body frame are given by

$$\vec{M}_{aero} = \left[T_B^{S_R}\right]^T \left[T_{S_R}^{W_R}\right]^T \vec{M}_{Rwing} + \left[T_B^{S_L}\right]^T \left[T_{S_L}^{W_L}\right]^T \vec{M}_{Lwing} \tag{4.19}$$

4.4 Governing Equations of Motion

The equations of motion are now summarized for the FWMAV. Since mass of wings is less than 3% of the total body mass, the inertial effects due to wings mass are neglected in the equations of motion. The translational kinematics equation is given by

$$\dot{\vec{X}} = \left[T_I^B\right]^T \vec{U} \tag{4.20}$$

The translational dynamics equation is given by

$$\vec{F}_{\text{aero}} + m_{\text{total}} T_{\text{I}}^{\text{B}} \vec{g} = m_{\text{total}} \left(\dot{\vec{U}} + \vec{\Omega} \times \vec{U}\right) \tag{4.21}$$

The rotational kinematics equation is given by

$$\dot{\vec{Q}} = \begin{bmatrix} 0 & -\vec{\Omega} \\ \vec{\Omega} & -\vec{\Omega}\times \end{bmatrix} \vec{Q} \tag{4.22}$$

The rotational dynamics equation is given by

$$\vec{M}_{\text{aero}} = \vec{\Omega} \times I_{\text{body}}\vec{\Omega} + I_{\text{body}}\dot{\vec{\Omega}} \tag{4.23}$$

These equations will be used in the open loop simulation of the FWMAV.

CHAPTER 5

OPEN LOOP SIMULATION

5.1 Simulation Inputs

The wing kinematics for the FWMAV model is taken from Azuma [38]. The flapping angle of the wing is given by

$$\zeta(t) = \zeta_0 + \zeta_1 \sin(\omega t), \tag{5.1}$$

where $\omega = 2\pi f$, f being the wing flapping frequency. The stroke amplitude of a fruit-fly is 160 deg. Therefore $\zeta_1 = 80°$. The deviation angle is given by

$$\beta(t) = \beta_0 + \beta_1 \sin\left(\omega t - \frac{\pi}{2}\right) \tag{5.2}$$

The deviation angle is set at 0 deg for the simulation runs. The wing pitch angle is given by

$$\theta(t) = \theta_0 + \theta_1 \sin(\omega t) \tag{5.3}$$

The properties of the flapping wing MAV model are listed in table 5.1.

Table 5.1. Properties of MAV model

Property	Value
Mass of body, m_{body}	$1736e^{-6}$ g
Mass of each wing, $m_{wingR,L}$	$57e^{-6}$ g
Wing semi-span, b	0.3 cm
Wing maximum chord, $chord_{max}$	0.12 cm
Wing Flapping Frequency, f	240 Hz
Stroke Amplitude	160 deg

Since the inertial effects due to mass of the wings are neglected in this study, the inertia tensors for the wings will not be considered. The inertia tensors of the body are listed in table 5.2.

Table 5.2. Body Inertia Tensors of MAV model

Inertia I_{Bii}	Value in $gm - cm^2$
I_{Bxx}	$3e^{-6}$
I_{Byy}	$12e^{-6}$
I_{Bzz}	$13e^{-6}$
I_{Bxy}	0
I_{Byz}	0
I_{Bxz}	$-4.36488e^{-8}$

5.2 Open Loop Simulation Studies

Open loop simulation study was conducted using modeling and simulation software Simulink. Six cases were simulated for the different combinations of wing angle values. Since all the scenarios deal with symmetric flapping, the left and the right wing angles were set at same values. The cases were run for a simulation time of 60 flapping cycles. Table 5.3 lists the values of angles considered for the simulation cases. The simulations were run subject to initial conditions of flapping wing MAV starting at a height of 5 meters with a forward velocity of 1 m/s. The quaternions were initialized at [1,0,0,0], which is the standard intial value for no rotation.

5.2.1 Discussion on the choice of Dynamic Model Solver

A dynamic system is simulated by computing its states at successive time steps over a specified time span, using information provided by the model. The process of computing the successive states of a system from its model is known as solv-

Table 5.3. Open Loop Simulation Cases

Case	ζ_0 (deg)	ζ_1 (deg)	β_0 (deg)	β_1 (deg)	θ_0 (deg)	θ_1 (deg)	θ_s (deg)	χ (deg)
1	0	80	0	0	-90	0	90	0
2	0	80	0	0	90	0	0	0
3	0	80	0	0	-90	0	0	0
4	0	80	0	0	10	0	0	0
5	0	80	0	0	-10	0	90	0
6	0	80	0	0	0	60	0	0

ing the model. Two types of such solvers are provided by Simulink; fixed-step and variable-step. Both solvers use numerical techniques to compute the states at the next simulation time by proceeding with a time step. With a fixed-step solver, the time step size remains constant throughout the simulation, while with a variable-step solver, the step size varies from step to step, depending on the model dynamics. In the case of this research, a variable time step solver was preferred so that it would adjust the step size to the rapidly changing states of the dynamics and other discontinuities.

Variable step solvers are further classified as discrete or continuous step solvers. Continuous solvers are used when the model has continuous states, while discrete solvers are used when the states are absent or are discrete. Moreover, the solvers use numerical methods to for computation. Sometimes, the step size of the computation interval becomes extremely small and makes these methods numerically unstable, causing the equations of the dynamics to be stiff. For such cases, it is better to use stiff or implicit solvers. Since the states of the dynamic system considered for the research are continuous, a single step variable implicit solver 'ode23s' based on a second order modified Rosenbrock formula was chosen as it allows for crude error tolerances. A relative tolerance of $1e^{-12}$ was used for all the simulations.

5.3 Simulation Results

The simulation data obtained from the 6 cases was post-processed using MATLAB. MAV instantaneous and average positions, inertial and body velocities, instantaneous and average forces and moments, body angle of attack and side-slip angle, inertial x-z position and the Euler angles and angular rates were determined for each case. The Euler angles were calculated from the quaternions using the following equation.

$$\begin{bmatrix} \Phi \\ \Theta \\ \Psi \end{bmatrix} = \begin{bmatrix} \arctan\left\{\frac{2(q_0\, q_1 + q_2\, q_3)}{1-2\left(q_1^2+q_2^2\right)}\right\} \\ \arcsin\left\{2\left(q_0\, q_2 - q_3\, q_1\right)\right\} \\ \arctan\left\{\frac{2(q_0\, q_3 + q_1\, q_2)}{1-2\left(q_2^2+q_3^2\right)}\right\} \end{bmatrix} \tag{5.4}$$

Results obtained are depicted in 6 figures for each of the cases and will be discussed on a case by case basis. In all the cases the z-direction position was plotted with a negative scale so that it is positive upwards. Rest all values in z-direction are positive downwards since the z-axis is defined in that sense.

1. Case 1: $\zeta_1 = 80°$; $\theta_0 = -90°$; $\theta_s = 90°$

   This scenario is for the up and down motion of the wings. At first the wings are rotated through a negative constant wing pitch angle of 90 deg and then the stroke plane angle is turned by the same amount in the upward direction, which is positive rotation. From fig 5.1 we can see that the flapping wing MAV moves ahead slightly in the inertial x-direction before coming back to its original position, while it sinks gradually by around 9 cm in z-direction after starting from a height of 5 meters which can be found by the inertial velocity in z-direction as well. The inertial velocity in the x-direction keeps on reducing which means

that the MAV will tend to move further backwards. This can be seen in the x-z inertial position plot in fig 5.2. We can also see in this figure that the MAV angle of attack increases upto a value of 90 deg and starts decreasing in the negative region. Due to symmetrical flapping, there is no change in the position and velocity in y-direction as well as the sideslip angle. Fig 5.3 shows aerodynamic forces in x and z directions and the pitching moment having a periodic pattern, with no force production in y-direction and net zero rolling and yawing momemts as they are balanced out by the left and right wings. Fig 5.4 shows the body euler rolling and yawing angles Φ and Ψ respectively changing sign as the pitching angle Θ reaches its limiting value of ± 90 deg. This is only due to the singularity at that value, since we can see from the subplots that there is no change in either rolling or yawing rate. Figures 5.5 and 5.6 show the cyclic averaged forces, moments and positions of MAV.

2. Case 2: $\zeta_1 = 80°$; $\theta_0 = 90°$; $\theta_s = 0°$

   This scenario is for the forward and backward sweep motion of the wings in the horizontal plane. Here the wings are rotated through a positive constant wing pitch angle of 90 deg while the stroke plane angle is maintained at 0 deg. As seen in fig 5.7 MAV moves ahead and upwards with increasing amplitude in both directions. We can see from fig 5.8 that MAV is actually spiralling forward with a gain in height. The angle of attack plot shows a discontinuity around 0.08 seconds. Fig 5.10 shows that the body pitching angle encounters singular points more frequently than in the earlier case. Figures 5.9 and 5.11 show the forces and moments stabilizing at specific values. Fig 5.12 shows the average MAV positions.

3. Case 3: $\zeta_1 = 80°$; $\theta_0 = -90°$; $\theta_s = 0°$

   This scenario is also for the forward and backward sweep motion of the wings in the horizontal plane, albeit with a constant negative wing pitch angle of 90 deg, which means that the wing is flapping in reverse sense. The behavior of the flapping wing MAV is similar to the previous case with positive pitch horizontal flapping, but as seen in fig 5.13 and fig 5.14 MAV gains more height and moves ahead with a tighter spiral. We can also see in fig 5.14 in the angle of attack plot that discontuinity occurs at two places.

4. Case 4: $\zeta_1 = 80°$; $\theta_0 = 10°$; $\theta_s = 0°$

   In this run, the MAV is given a constant wing pitch angle of 10 deg as it flaps in the horizontal stroke plane. As seen from fig 5.19 MAV oscillates in x and z-directions wit ha very small amplitude, practically not moving at all. Fig 5.20 shows MAV spiralling becomes tighter in inertial x-z frame. Angle of attack plot shows dicontinuities at 8 points.Also MAV spirals 8 times, which means that everytime spiralling occurs, MAV angle of attack goes through a discontinuity. This can be corroborated by looking at angle of attack and inertial x-z frame plots for the earlier cases.

5. Case 5: $\zeta_1 = 80°$; $\theta_0 = -10°$; $\theta_s = 90°$

   In this run, the MAV is given a constant wing pitch angle of -10 deg and then the stroke plane angle is turned by a positive angle of 90 deg. Figures 5.25 to 5.30 show that the MAV behaves in the same way as in case 1 with very little change in the magnitude of the parameter values. This means that a 10 deg change in the pitching angle value for a vertically flapping MAV has no

significant effect on its dynamics.

6. Case 6: $\zeta_1 = 80°$; $\theta_0 = 0°$; $\theta_1 = 60°$; $\theta_s = 0°$

   In this case, the MAV wing is pitching at an amplitude of 30 deg, with the constant pitch angle and the stroke plane angle set to 0 deg. Fig 5.31 shows that the MAV moves ahead by 7 cm. It moves up by around 2 cm while behaving oscillatory, as can be seen in the inertial x-z frame plot in fig 5.32. Fig 5.34 shows pitching angle with alternate phase shifts. fig 5.33 shows the periodic behavior of the aerodynamic forces and moments, while fig 5.35 and fig 5.36 show the average plots.

5.4 Remarks

It can be noted from the the simulations that though most of the parameters studied in the plots were bounded, some of them showed erratic behavior, especially the body angle of attack and body pitching angle. This could be due to the fact that the aerodynamic expressions given by eq (4.15), which are used for the forces and moments calculations are making the system unstable. So the aerodynamic model taken from Dickinson et al. [29] might not be the best option to the study the nonlinear dynamics of the flapping MAV and should therefore be replaced.

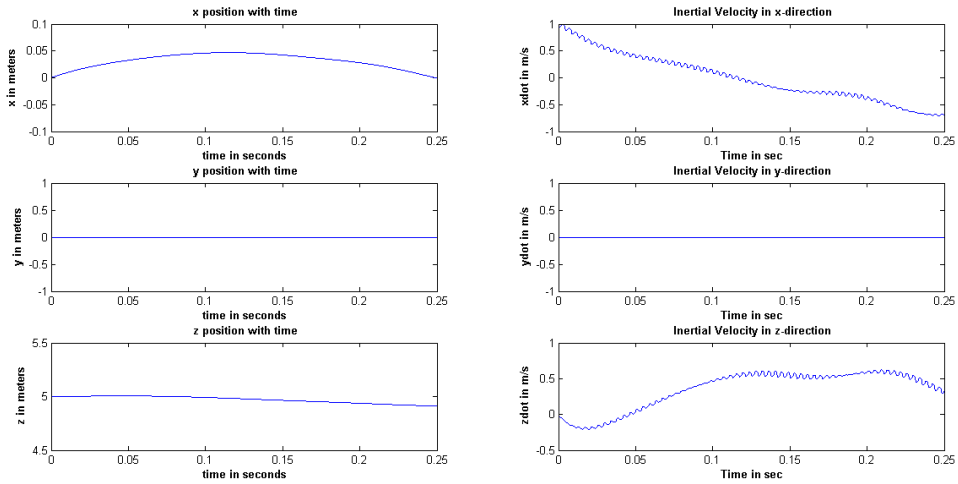

Figure 5.1. Case 1 inertial positions and velocities.

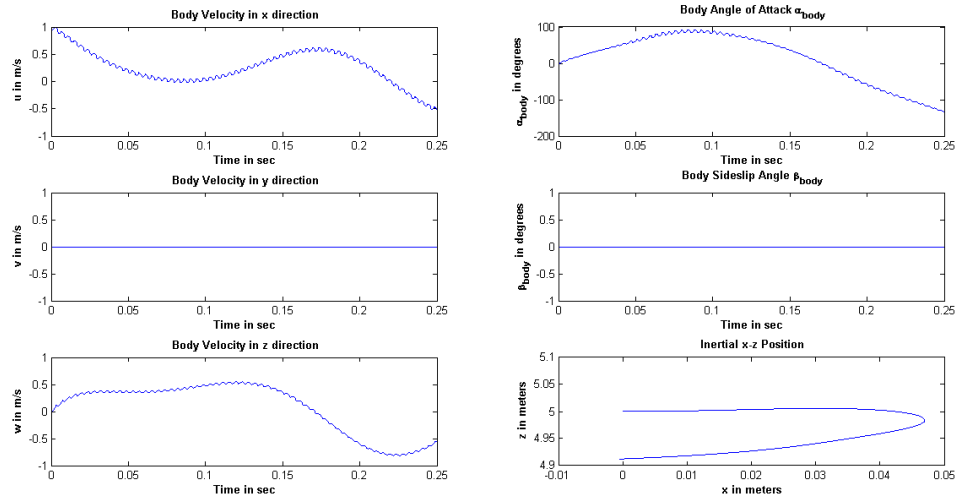

Figure 5.2. Case 1 body velocities, angle of attack, sideslip angle and inertial x-z position.

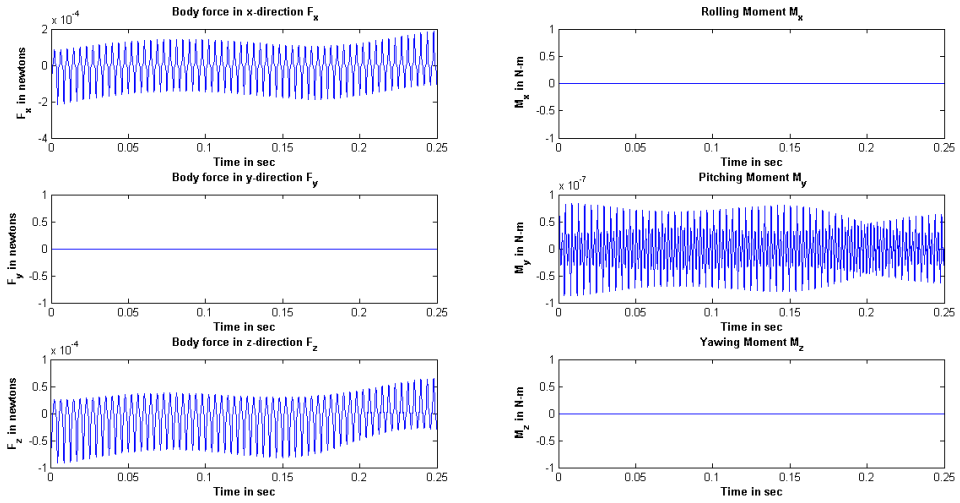

Figure 5.3. Case 1 aerodynamic forces and moments.

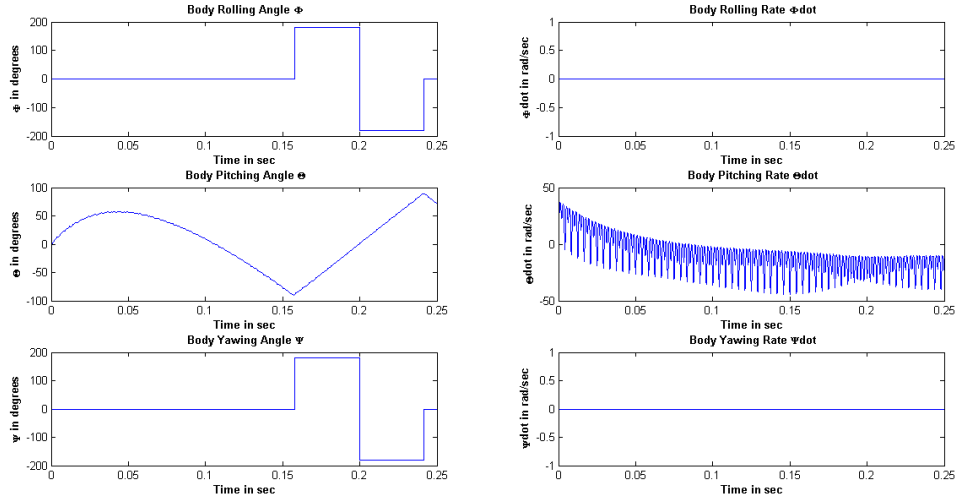

Figure 5.4. Case 1 Euler angles and angular rates.

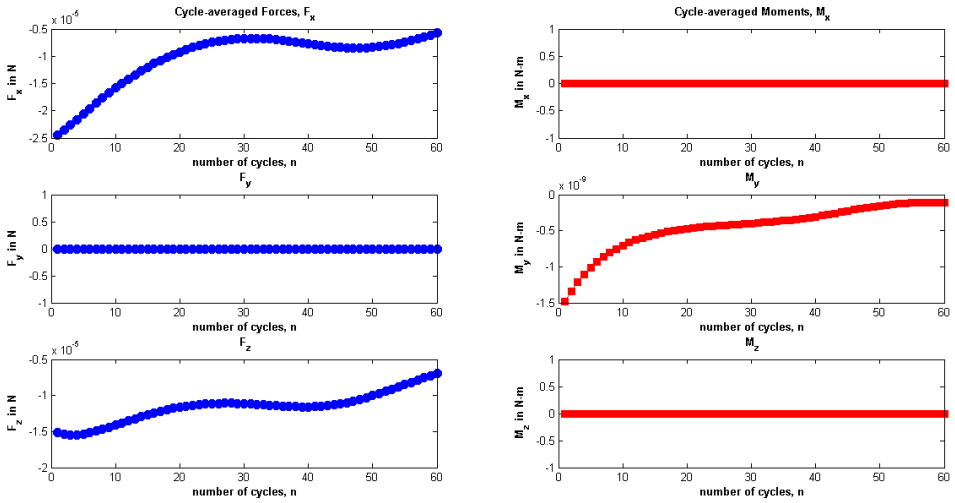

Figure 5.5. Case 1 cycle averaged forces and moments.

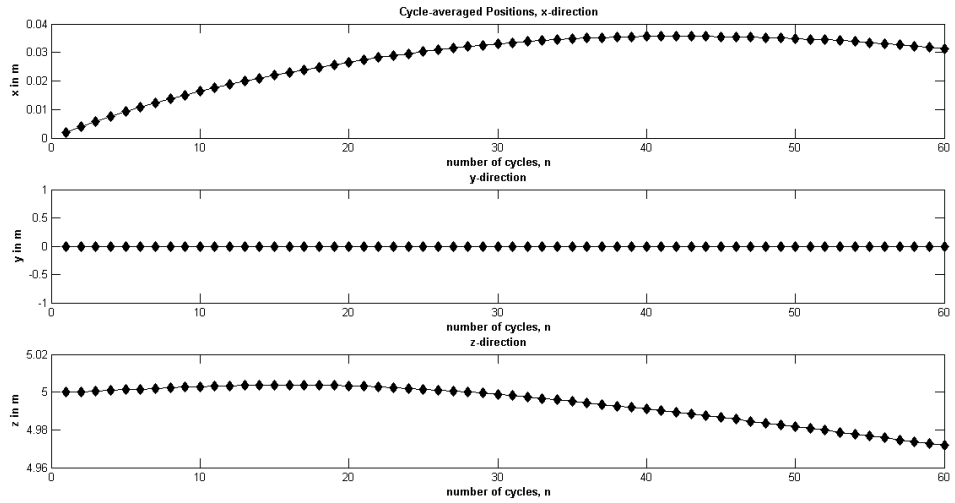

Figure 5.6. Case 1 cycle averaged positions.

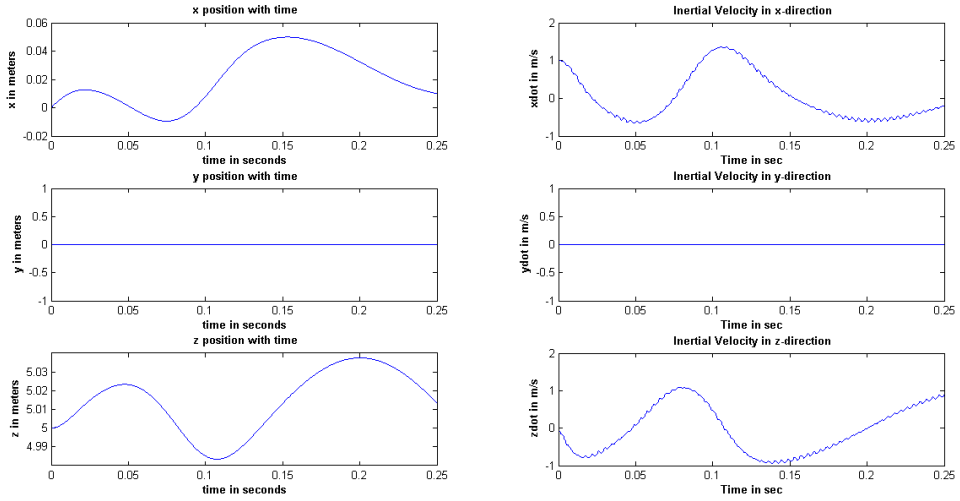

Figure 5.7. Case 2 inertial positions and velocities.

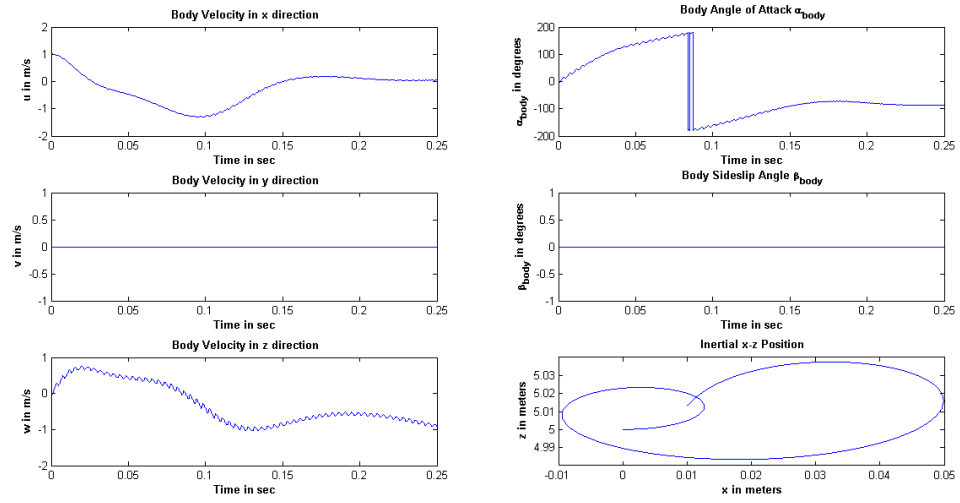

Figure 5.8. Case 2 body velocities, angle of attack, sideslip angle and inertial x-z position.

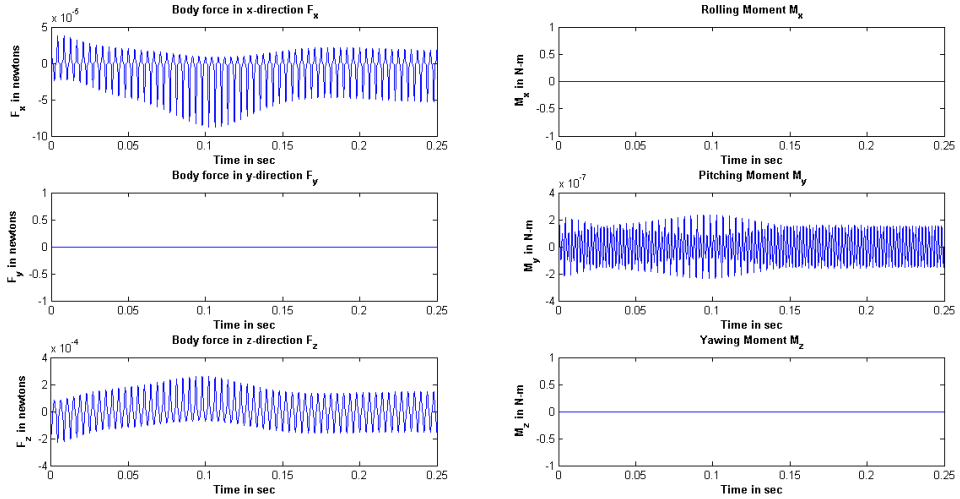

Figure 5.9. Case 2 aerodynamic forces and moments.

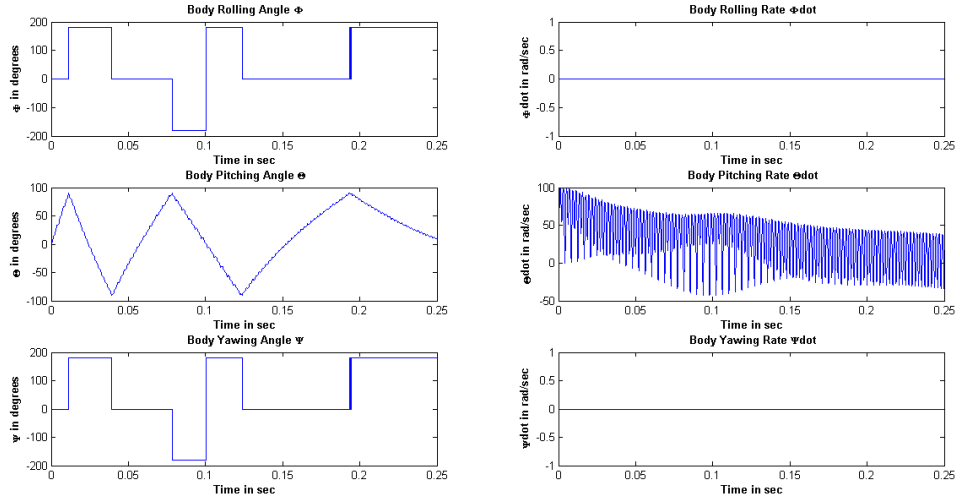

Figure 5.10. Case 2 Euler angles and angular rates.

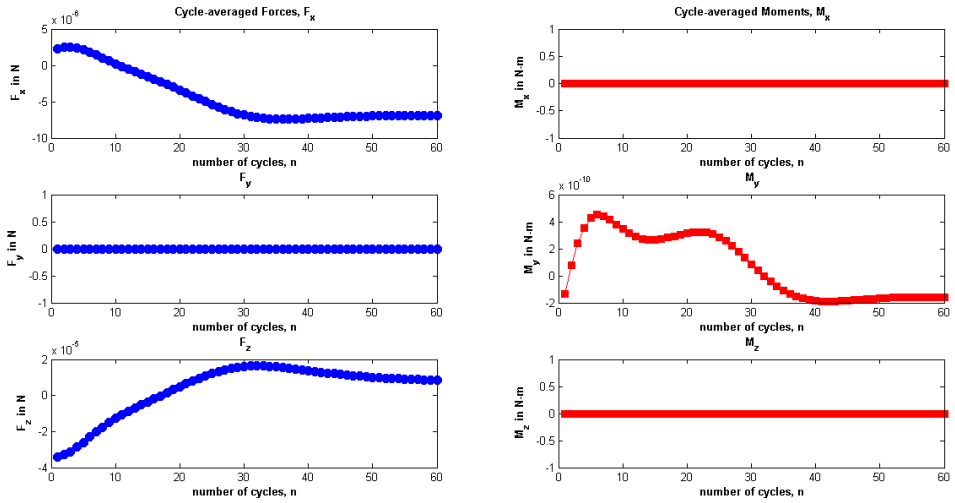

Figure 5.11. Case 2 cycle averaged forces and moments.

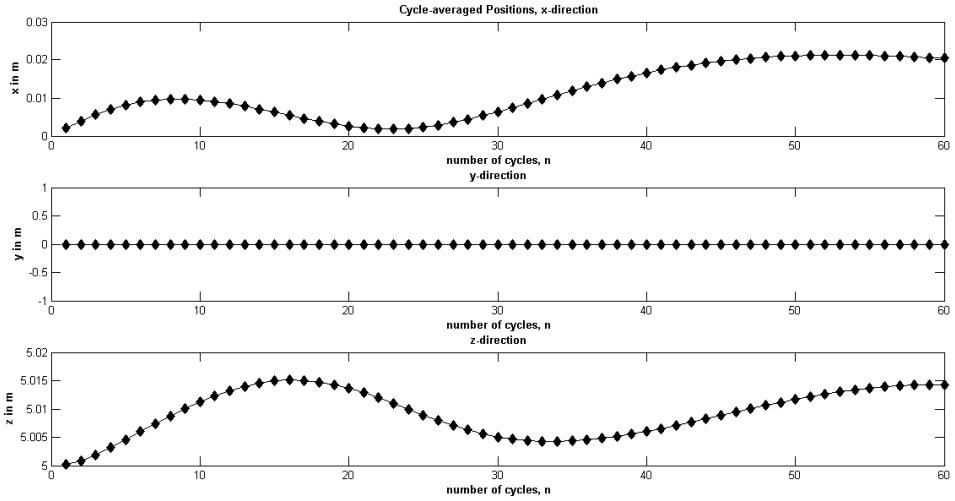

Figure 5.12. Case 2 cycle averaged positions.

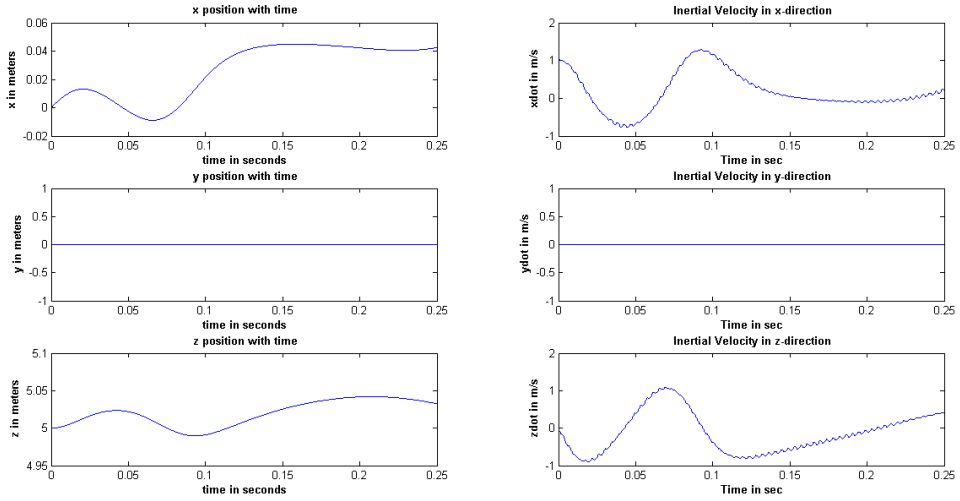

Figure 5.13. Case 3 inertial positions and velocities.

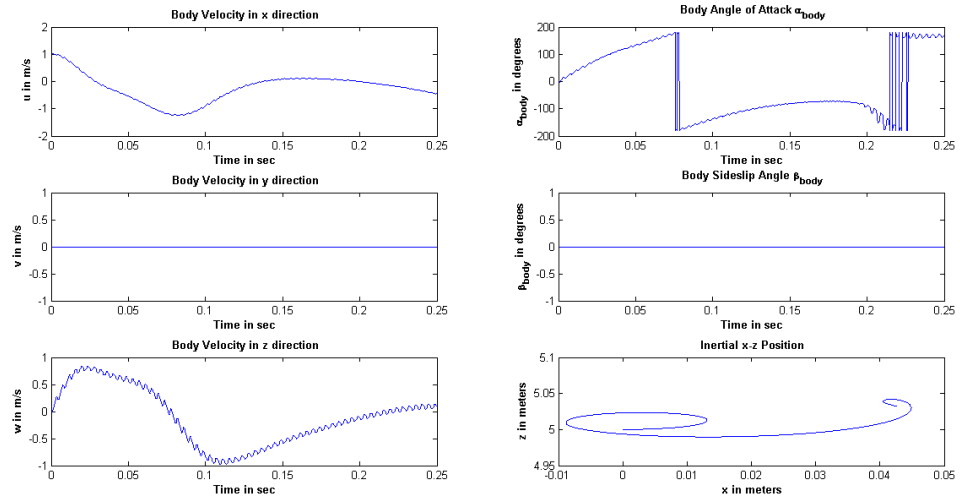

Figure 5.14. Case 3 body velocities, angle of attack, sideslip angle and inertial x-z position.

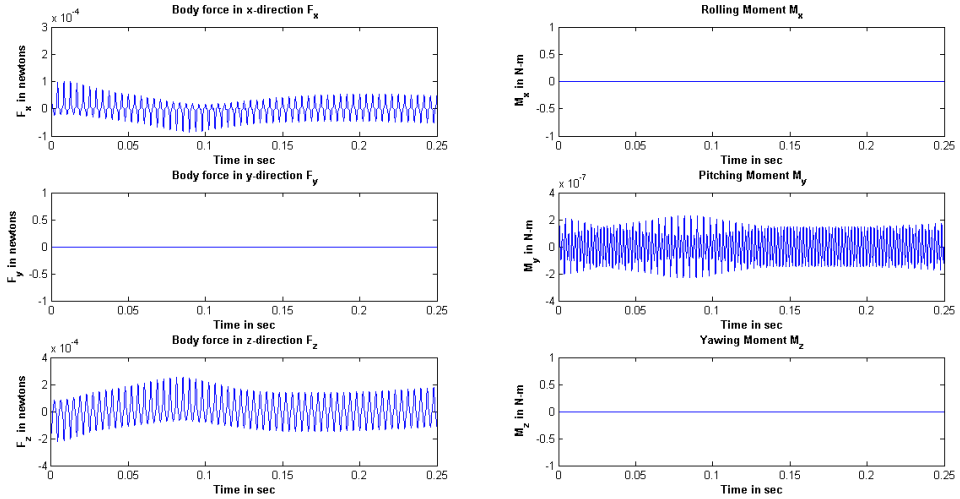

Figure 5.15. Case 3 aerodynamic forces and moments.

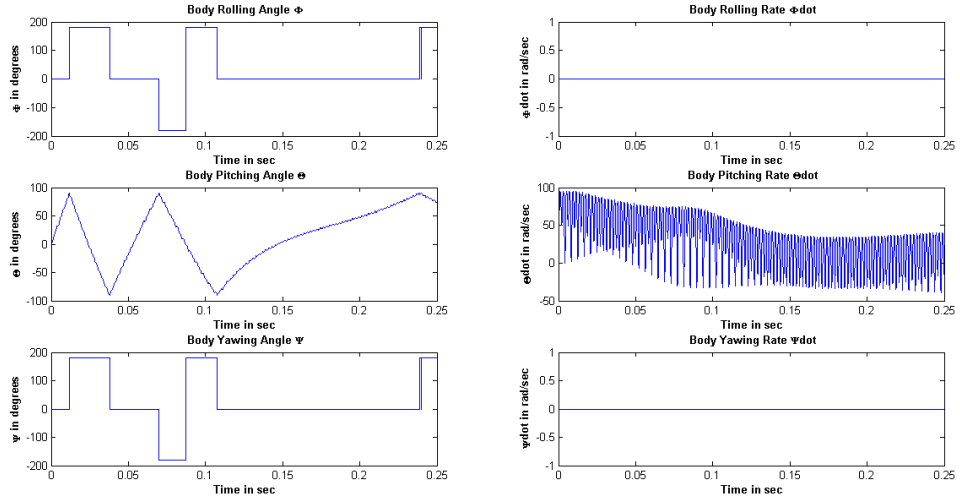

Figure 5.16. Case 3 Euler angles and angular rates.

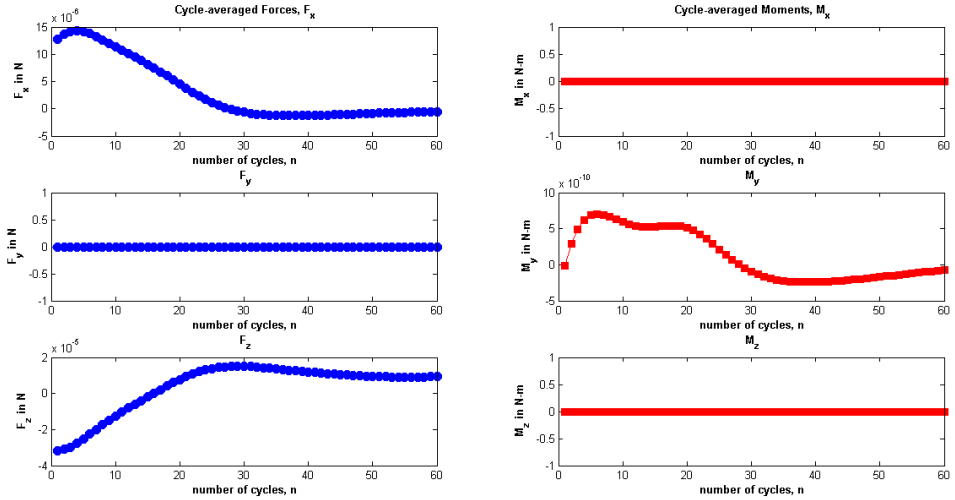

Figure 5.17. Case 3 cycle averaged forces and moments.

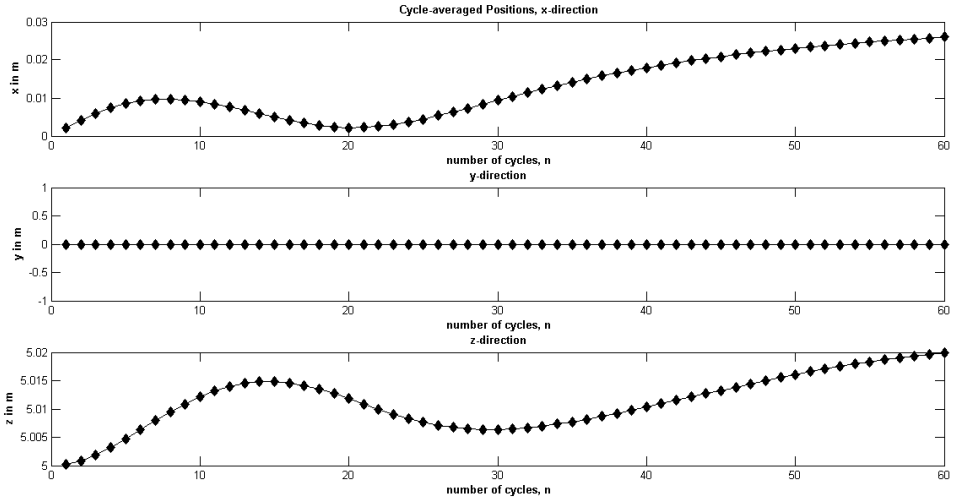

Figure 5.18. Case 3 cycle averaged positions.

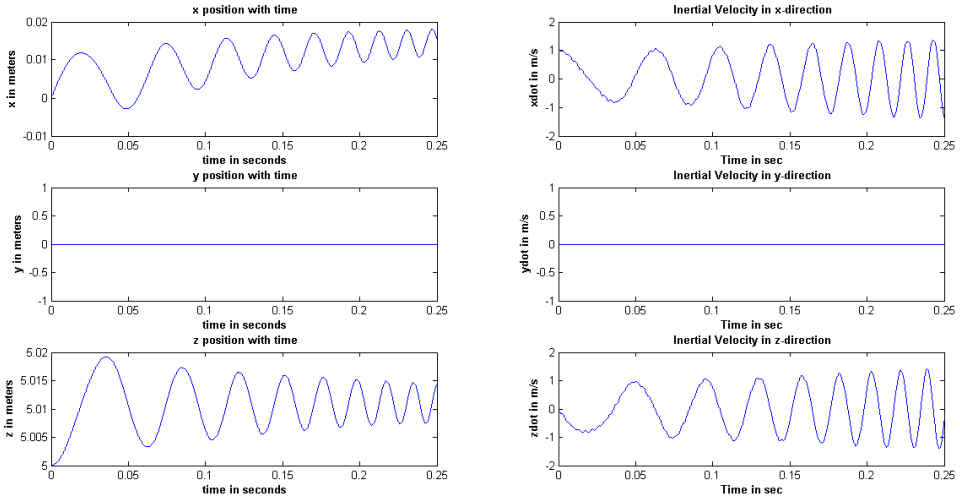

Figure 5.19. Case 4 inertial positions and velocities.

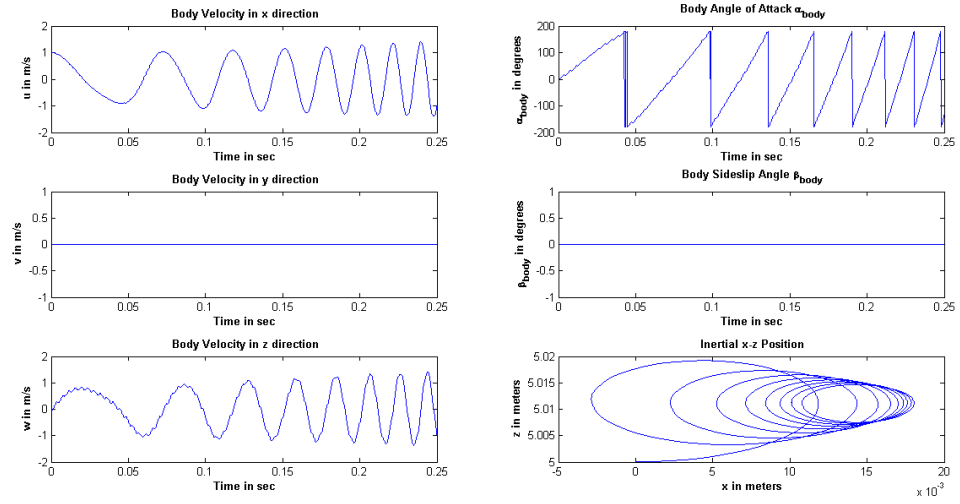

Figure 5.20. Case 4 body velocities, angle of attack, sideslip angle and inertial x-z position.

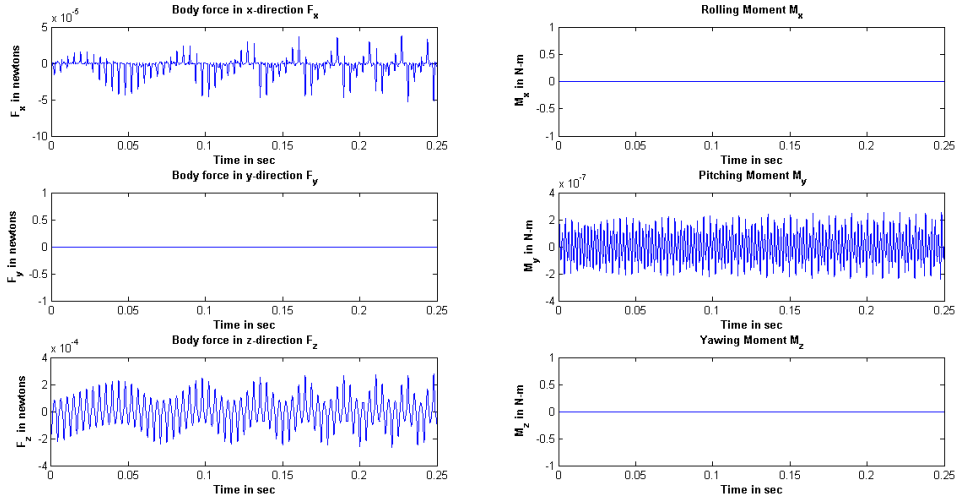

Figure 5.21. Case 4 aerodynamic forces and moments.

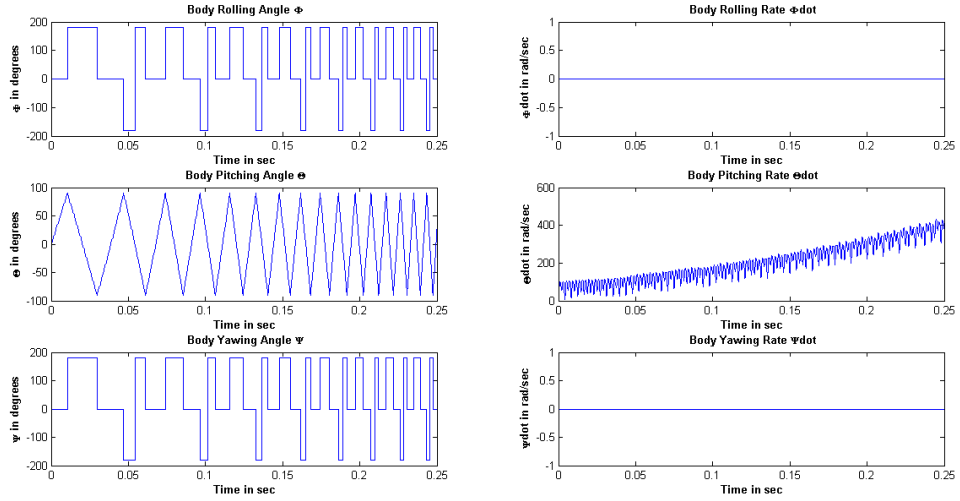

Figure 5.22. Case 4 Euler angles and angular rates.

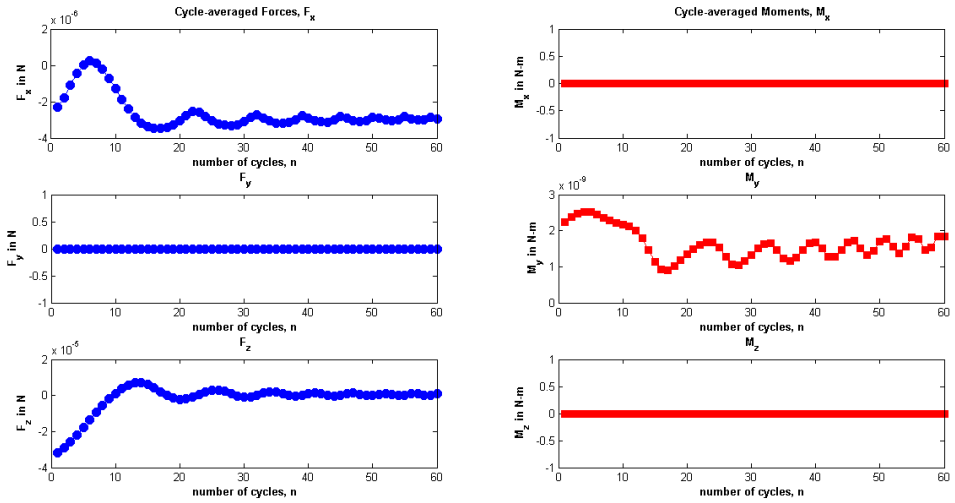

Figure 5.23. Case 4 cycle averaged forces and moments.

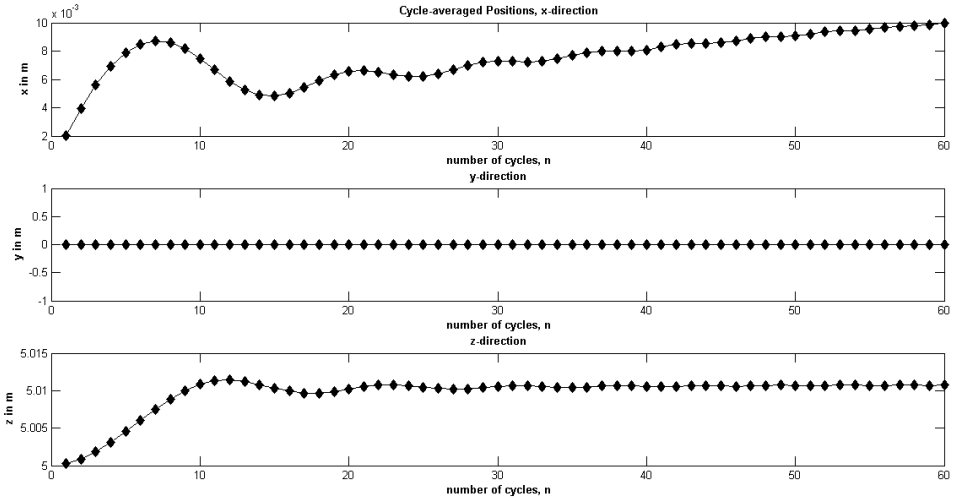

Figure 5.24. Case 4 cycle averaged positions.

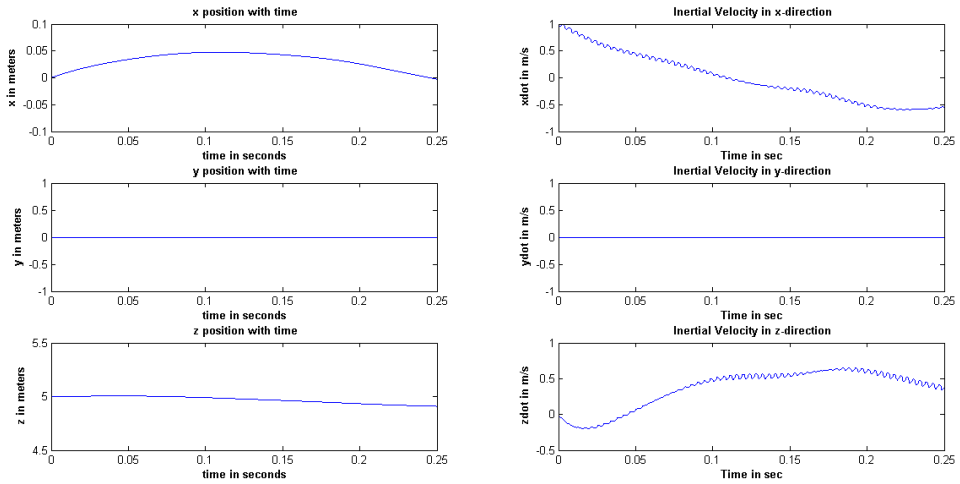

Figure 5.25. Case 5 inertial positions and velocities.

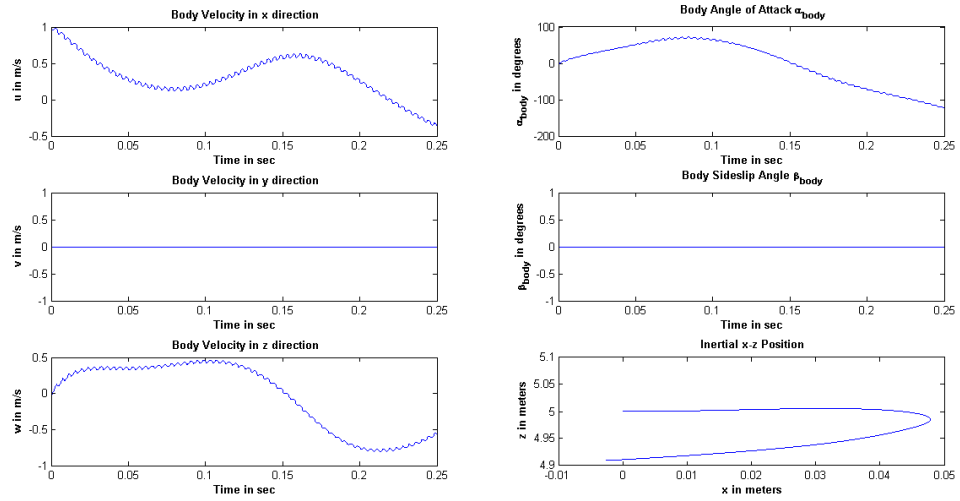

Figure 5.26. Case 5 body velocities, angle of attack, sideslip angle and inertial x-z position.

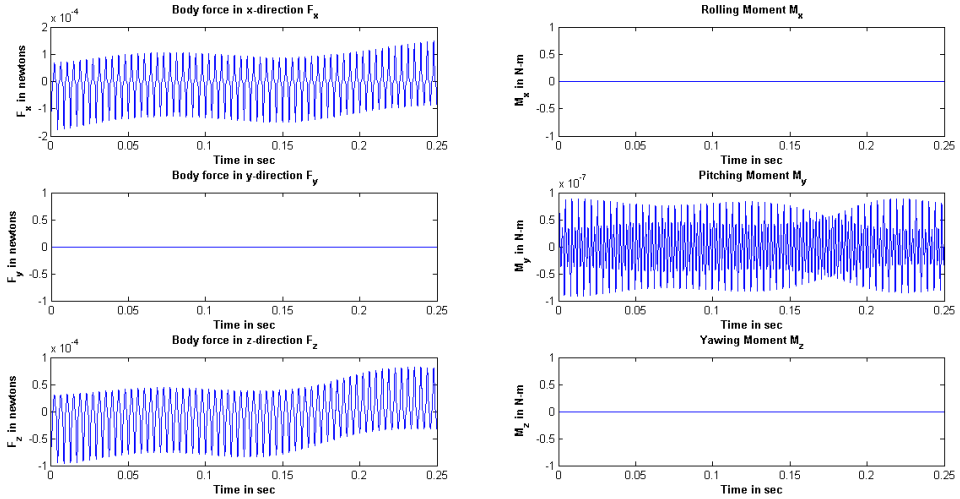

Figure 5.27. Case 5 aerodynamic forces and moments.

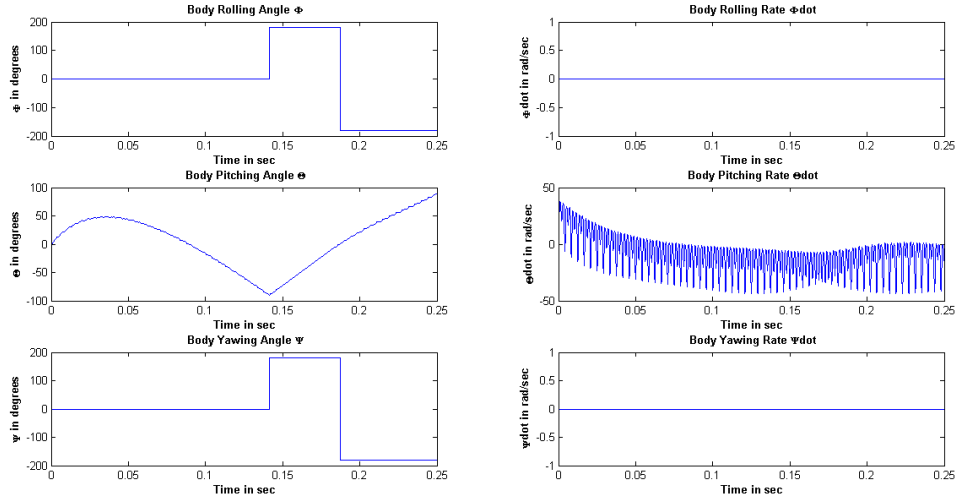

Figure 5.28. Case 5 Euler angles and angular rates.

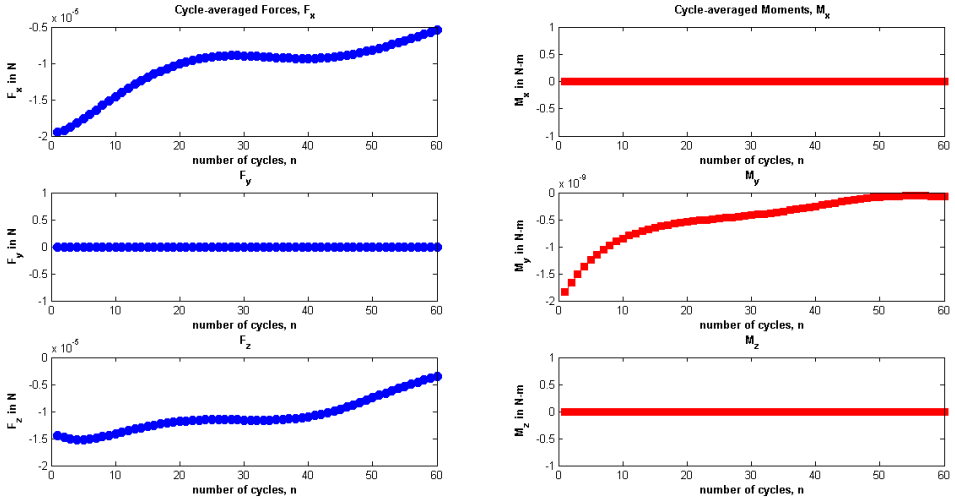

Figure 5.29. Case 5 cycle averaged forces and moments.

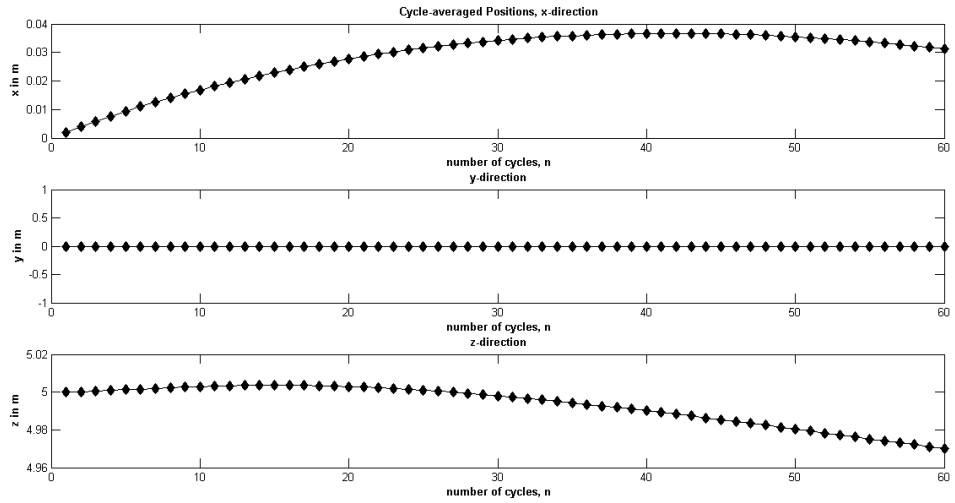

Figure 5.30. Case 5 cycle averaged positions.

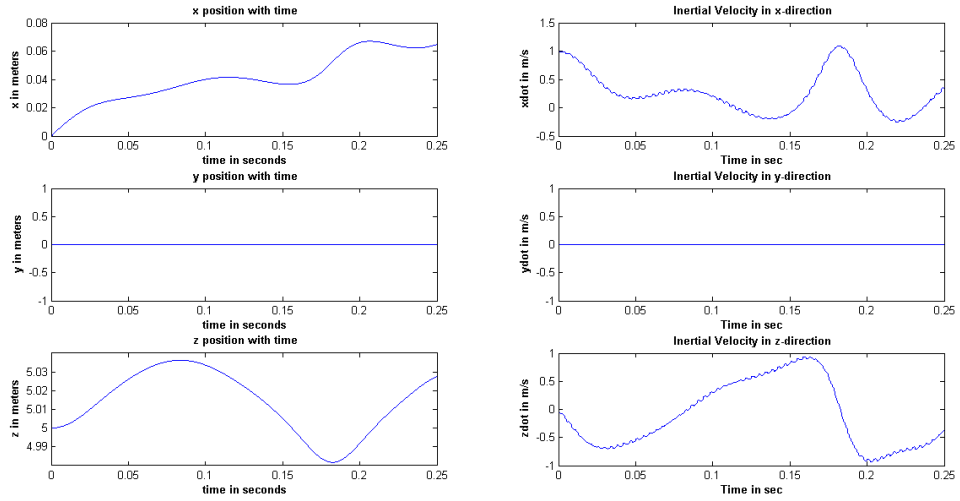

Figure 5.31. Case 6 inertial positions and velocities.

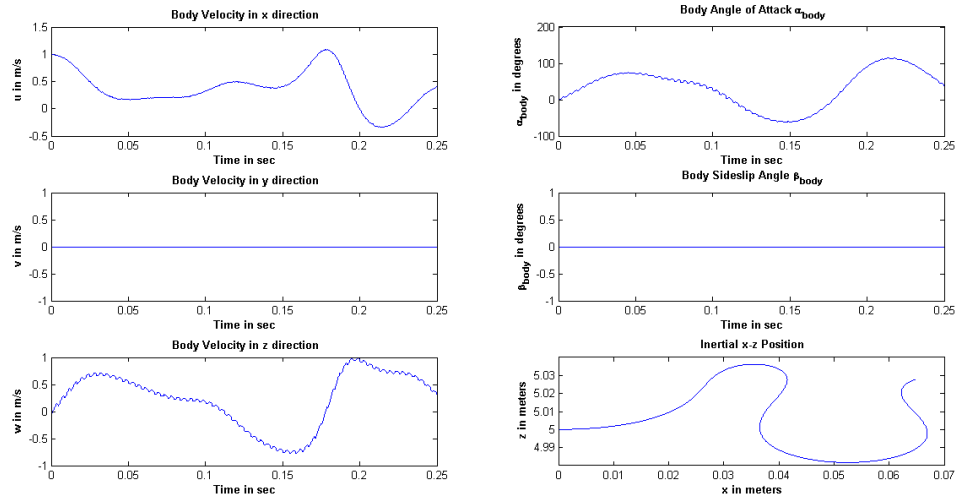

Figure 5.32. Case 6 body velocities, angle of attack, sideslip angle and inertial x-z position.

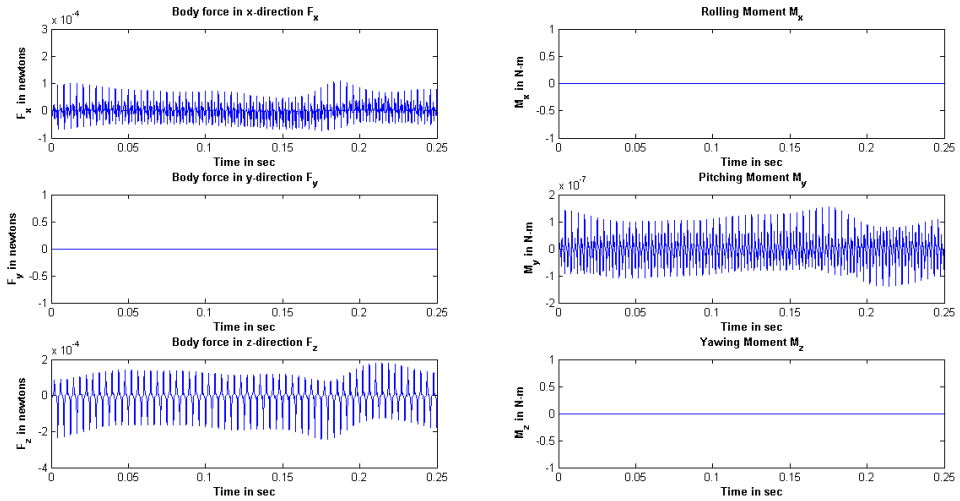

Figure 5.33. Case 6 aerodynamic forces and moments.

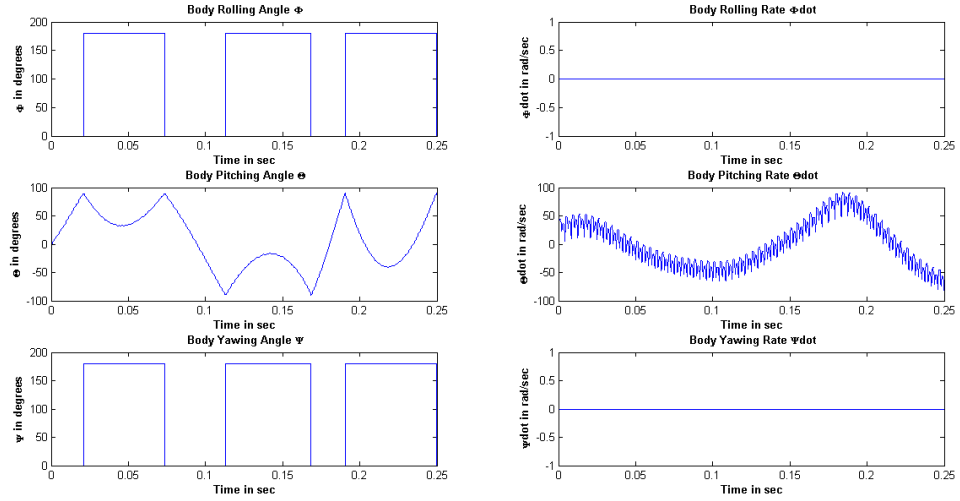

Figure 5.34. Case 6 Euler angles and angular rates.

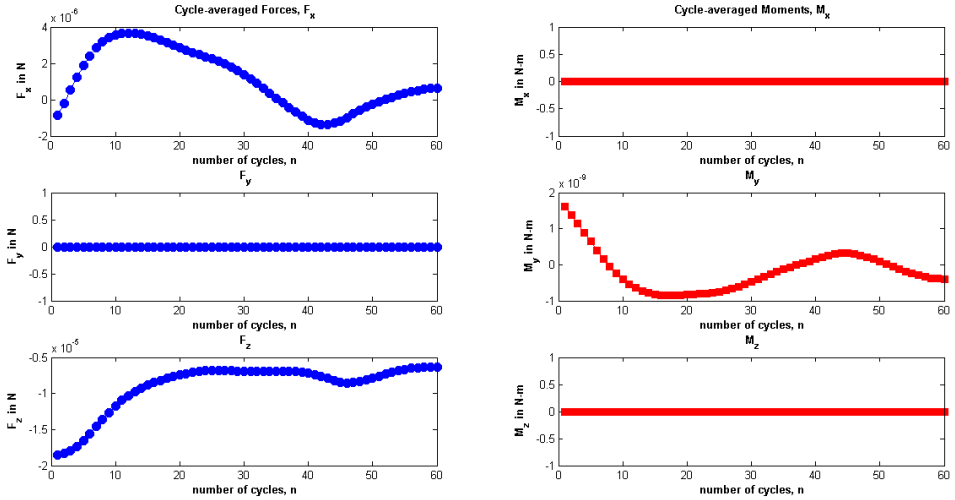

Figure 5.35. Case 6 cycle averaged forces and moments.

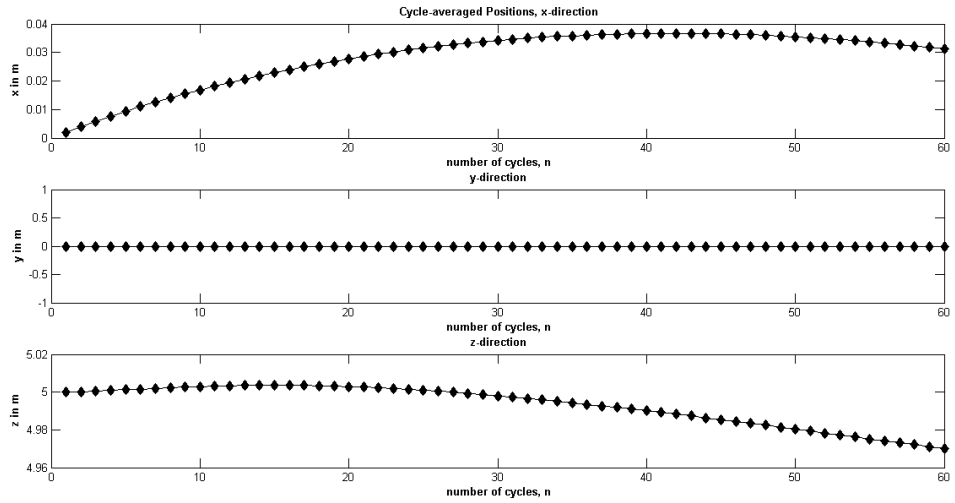

Figure 5.36. Case 6 cycle averaged positions.

CHAPTER 6

CFD ANALYSIS

6.1 Need for New Aerodynamic Parameters

The expressions for aerodynamic coefficients C_L and C_D mentioned in section 4.3 and developed by Dickinson et al. [29] to investigate the dynamics of insect flight were based on experimental setup for hover. The authors used a simple harmonic relationship to come up with a curve fit for the mean values of the aerodynamic co-efficients. The mean values were obtained by flapping the modeled wings at constant tip velocity for different values of pitch angle of attack, which was kept constant for each flapping run. Also, the values were calculated by averaging the instantaneous values over the interval which showed stable force trajectories. Wang et al. in [39] made use of a sinusoidal pitching angle of attack, but followed a similar procedure of curve fitting to obtain the expressions.

All this means that the utility of the derived expressions is limited to certain scenarios. Moreover, the expressions which were obtained from intermittent values of angle of attack,depend explicitly on it. This becomes a very important factor in the case of simulations of the nonlinear dynamics, where instantaneous values of angle of attack are being fed into the expressions to get the required aerodynamic co-efficients.

So there felt a need to come up with a consistent aerodynamic model to study the flight dynamics of micro air vehicle with a reasonably accurate representation of aerodynamic forces and moments. The expressions for aerodynamic coefficients obtained thereof would be functions of a new set of aerodynamic parameters.

6.2 Computational Fluid Dynamics Approach

In order to determine the aerodynamic variables that would be used in the new expressions, a thorough investigation of flow over flapping wing must be done. This thesis does not include the formulation of the new aerodynamic model discussed in the previous section. Rather a parametric study of the different flapping trajectories made by 2-D wing section of the MAV is performed using computational fluid dynamics (CFD) techniques. The procedure adopted for this study is as shown in the flow chart given in fig 6.1.

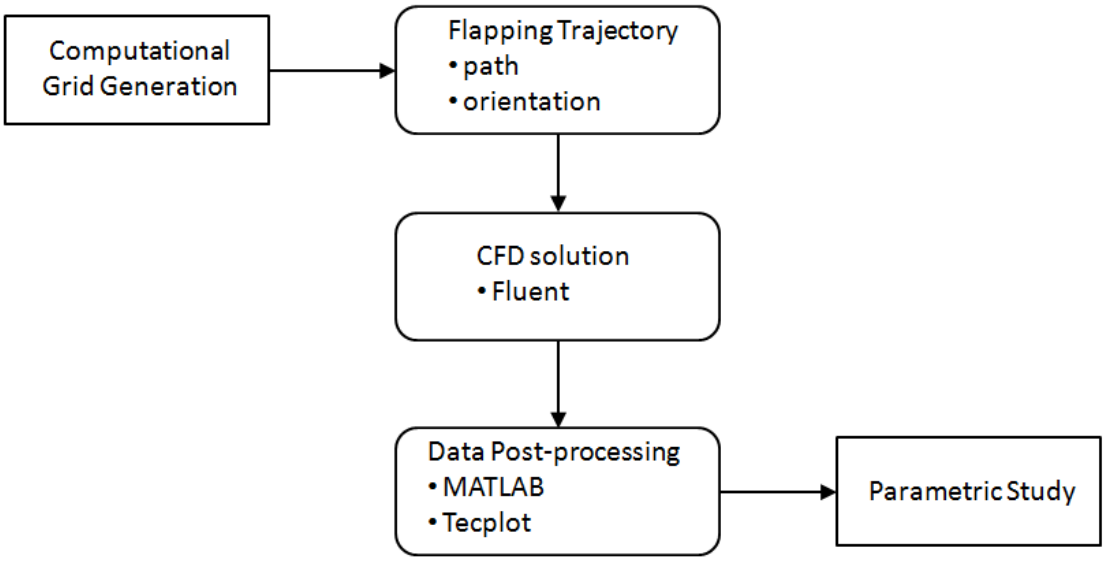

Figure 6.1. Flow chart for CFD analysis.

The following sections explain in detail the various steps taken to perform the parametric study of the different flapping paths.

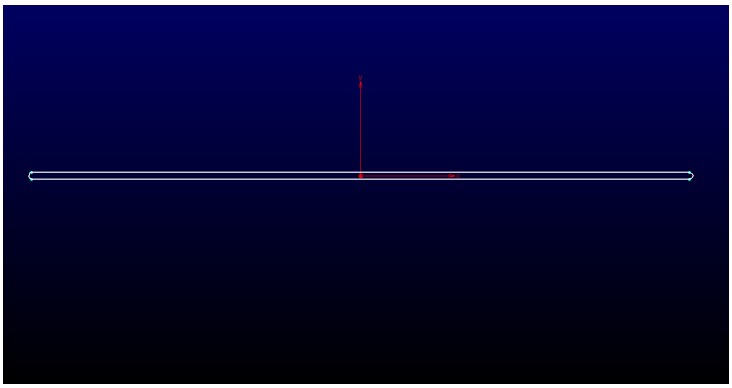

Figure 6.2. Model of a wing section used for CFD analysis.

6.2.1 Computational Grid

A good refined computational grid or mesh is very important for the accuracy of results obtained from the computational analysis. A mesh is called fine when the node or cell density in a region is more, and a coarse mesh is where it is less. Typically, mesh is kept finer in the region where the flow is highly unsteady and coarser where it has relatively less disturbance. It is also essential to avoid unnecesary use of fine mesh to save on computational time and power. Grid generation software Pointwise was used to make the required mesh.

Cross-section of a thin flat plate of length 1 mm and thickness 0.01 mm was used as a model for a wing section of the flapping wing MAV. The two edges of the model were blunted to avoid flow dettachment. The model was placed with its center coinciding with the origin of the workspace coordinate system, as shown in fig 6.2. 100 nodes were created on each side of the model, while each of the edges had 5 nodes for cell connectivity.

For the given problem, unstructured grid generation was preferred over structured, since unstructured grids reduce the overall complexity of the grid generation process. Unstructured grids also offer excellent parallel performance due to the ease

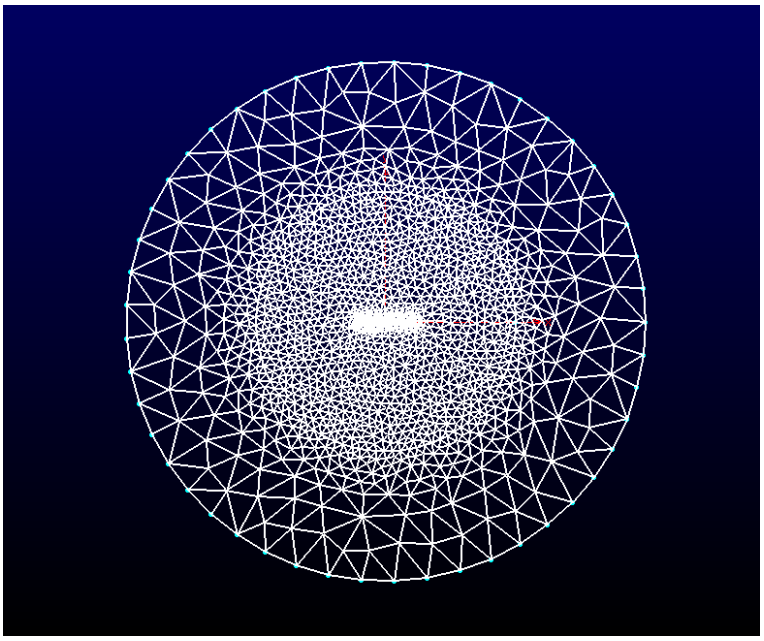

(a)

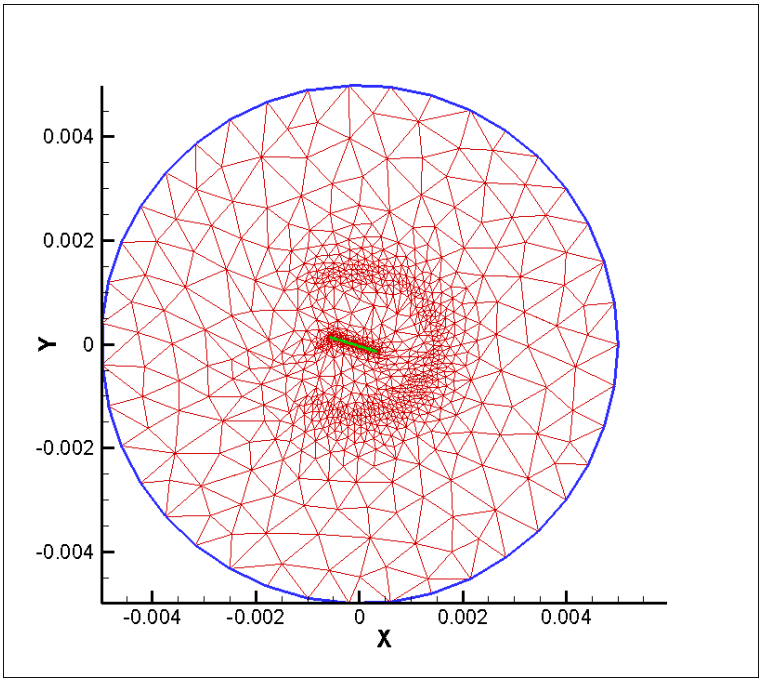

(b)

Figure 6.3. Initial computational domain with (a) Smaller grid size and (b) Coarse mesh.

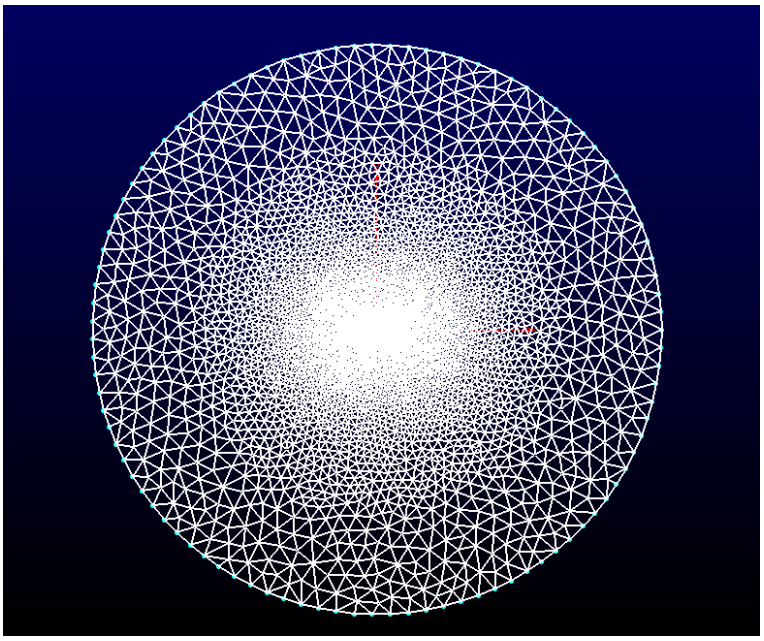

(a)

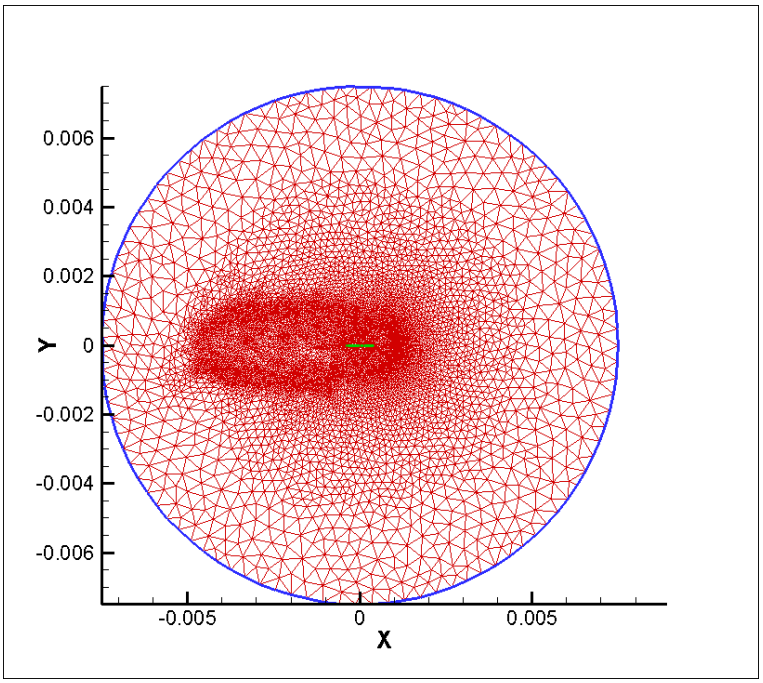

(b)

Figure 6.4. New computational domain with (a) Larger grid size and (b) Refined mesh.

of load balancing. The fact that the mesh is moving due to the motion of the flapping wing was also one of the reasons since the unstructured grids offer good grid adaptation properties. However, it is important to monitor the unstructured mesh schemes to check if there are high aspect ratio cells, since they add to the errors in the results.

The first task while creating a mesh is to define the dimension of the computational domain, which has to be large enough to not interfere with the results. Also, the mesh should be fine enough for a larger part around the model in order to keep the mesh resolution quality uniform with time. At first, an O-type grid with a diameter of 10 times the model length was created as shown in fig 6.3(a). 50 nodes were created on the connector forming the outer boundary of the domain. As seen from fig 6.3(b), the mesh resolution changed dramatically with time. The mesh which was finer in a region around the model became coarse. Such an unrefined mesh would not produce accurate results.

This grid was replaced by an improved O-type grid with a diameter of 15 times the model length and a total of 100 nodes on the outer boundary connector. A boundary decay factor of 0.99 was used to get smooth refined mesh as seen in fig 6.4(a). No high aspect ratio cells were found in the generated grid. Fig 6.4(b) shows that the grid has adapted very well with time and the mesh resolution quality is intact.

6.2.2 Flapping Trajectories

Insects rely on different flapping trajectories to produce the the required aerodynamic forces, in order to maintain their postion in case of hover, or to propel themselves to a new position. Broad study of this insect mechanism for producing forces is imperative to determine the required aerodynamic parameters accurately. Figures 6.5 to 6.8 show different wing flapping trajectories considered for the parametric study.

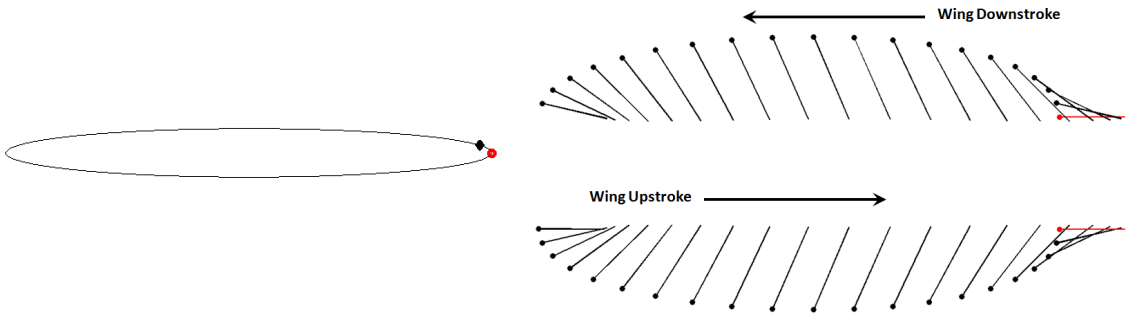

(a) (b)

Figure 6.5. Elliptical flapping trajectory with (a) Flapping direction and (b) Instantaneous wing positions.

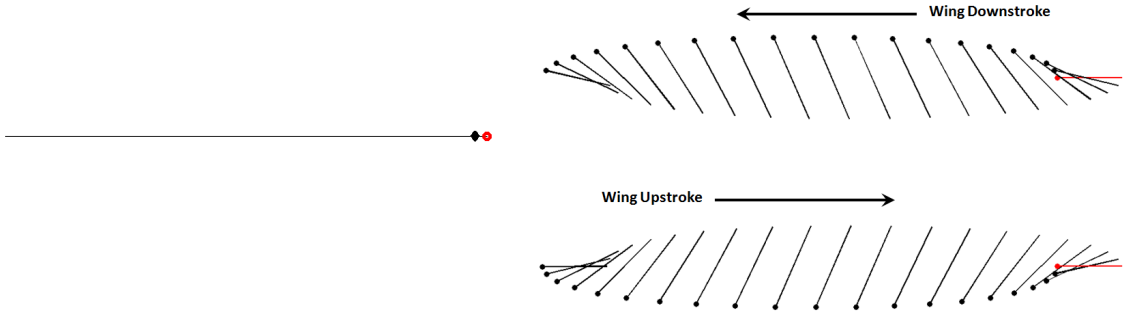

(a) (b)

Figure 6.6. Straight flapping trajectory with (a) Flapping direction and (b) Instantaneous wing flapping positions.

As seen in fig (a) for each of the trajectories, the circle and the diamond show the start and the direction of the wing stroke respectively. Fig (b) in each case shows the instantaneous wing positions during the two half strokes; the downstroke or the forward flapping motion of the wing, and the upstroke or the backward flapping motion. The circular head on the wing depicts the wing leading edge. All the paths were generated using parametric functions. In fig 6.8, a shaping factor was used to replicate the optimum flapping trajectory obtained by Ueno et al. in [2]. For

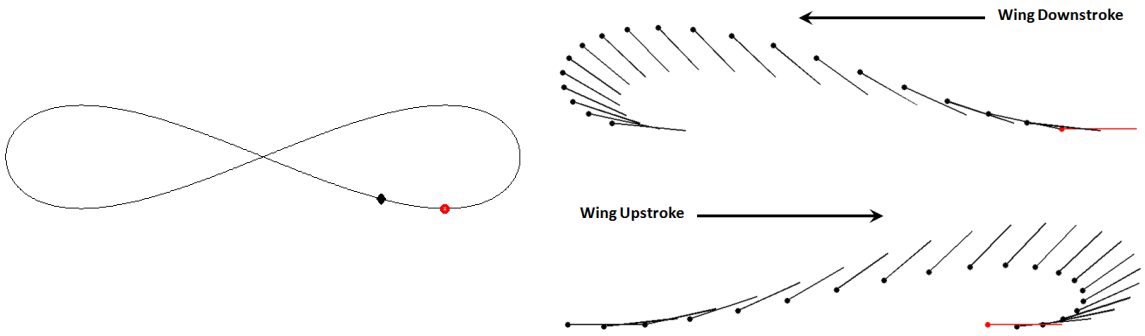

(a) (b)

Figure 6.7. Figure-8 flapping trajectory with (a) Flapping direction and (b) Instantaneous wing flapping positions.

uniformity, the stroke lengths for all the trajectories were kept same. The orientation of the trajectory is fixed parallel to the x-axis for the parametric study.

6.2.3 Computational Flow Solver

The commercial CFD program Fluent was used to solve the unsteady incompressible Navier-Stokes equations on an unstructured triangular mesh described earlier. A pressure-based implicit finite volume method with SIMPLE scheme and standard 1st-order upwinding was used to discretize the equations. A Green-Gauss cell-based gradient method was used to compute the gradient of the scalar at the cell faces and also for computing the secondary diffusion terms and velocity derivatives. The cell-center approach deals with less points over the domain as it stores the solution at each cell-center thereby taking less memory than the node-center approach. The discrete form of this method is written as

$$(\nabla\phi)_{c0} = \frac{1}{\nu}\sum_{f}\bar{\phi}_f\,\vec{A}_f, \tag{6.1}$$

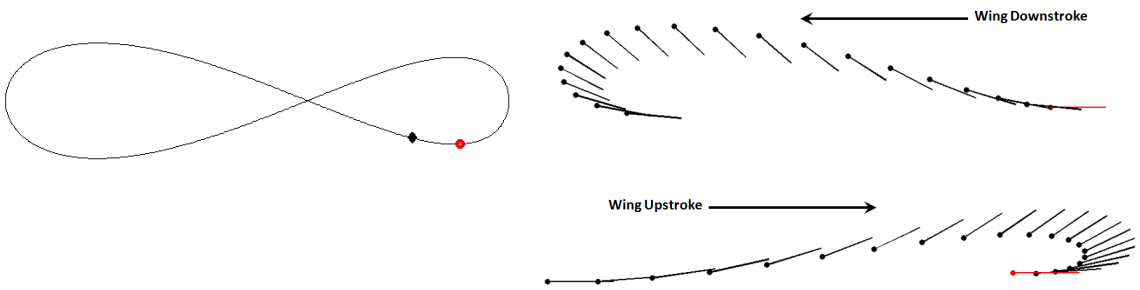

(a) (b)

Figure 6.8. Optimal flapping trajectory obtained by Ueno et al. [2] with (a) Flapping direction and (b) Instantaneous wing flapping positions.

where $\bar{\phi}_f$ is the value of the scalar ϕ at the cell face centroid $c0$. The summation is over all the faces enclosing the cell. The face value, $\bar{\phi}_f$, is taken from the arithmetic average of the values at the neigboring cell centers,i.e.,

$$\bar{\phi}_f = \frac{\phi_{c0} + \phi_{c1}}{2} \tag{6.2}$$

Unsteady Particle Tracking with fluid flow time step was used for the Discrete Phase Model to derive the equations for the underlying physics which are solved transiently during the solver run. A moving mesh scheme was used to allow for the wing motion relative to the fixed outer boundary. The wing motion was large relative to the mesh size so dynamic smoothing and remeshing schemes were emplyed at each time step to maintain a high quality mesh. For the remeshing method, the maximum length and maximum cell skewness were set to 0.0001 m and 0.6 respectively, while a size remesh interval of 5 was used. The details of smoothing parameters are given in table 6.1. Fig 6.9 shows an example of a moving mesh about the wing section with smoothing and remeshing employed.

Table 6.1. Smoothing Parameters for Dynamic Mesh of MAV model

Property	Value
Spring Constant Factor	0.1
Boundary Node Relaxation	0.1
Convergence Tolerance	0.001
Number of Iterations	20

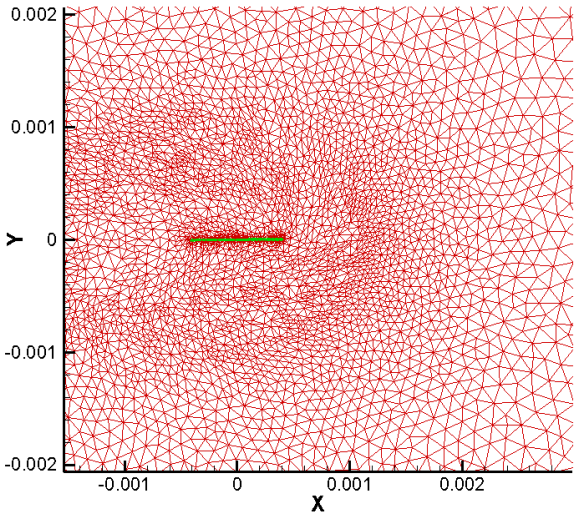

Figure 6.9. Unstructured mesh around the wing section with smoothing and remeshing employed.

Ueno et al. in [2] found that the number of time steps per cycle is a critical parameter. If the time step size is too large, the mesh adaptation sheme was found to fail. They observed in their preliminary experiments that 1000 time steps per cycle resulted in stable computation for all generated designs.

The unsteady lift produced by the wing section is computed by integrating the time-variant static pressure over the wing section during one cyclic motion. The reference values for calculation of lift coefficient C_L is given in table 6.2. While the wing section was set at a no-slip wall with the user-defined motion, the outer

boundary condition of the computational domain was set as a velocity inlet of 0.01 m/s in x-direction.

Table 6.2. Reference Values for calculation of Lift coefficient C_L

Property	Value
Area, S	$1m^2$
Density, ρ	1.225 kg/m^3
Velocity, V	1 m/s
Viscosity, μ	$1.7894e^{-5}kg/m\text{-}s$

Experiments were run for different cycles of flap, starting with 10 used by Ueno et al. in [2] to check if the unsteady lift coefficient became periodic. It was found that after 50 cycles, C_L becomes nearly periodic, and the time-averaged lift coefficient was obtained for the 51st cycle.

6.2.4 Data Post-processing

User-defined functions were used to intialize the solutions for the unstructured moving mesh. A file was created to define a wing section trajectory that would generate the input to flow solver for the mesh movement. An initialization file was created that would save the data history of the coefficients of lift, drag and moment C_L, C_D and C_m respectively for the entire solver runtime, as well as saving the Fluent case and data files every 50 timesteps only for the last cycle. A file was also written to calculate the average lift coefficient C_{Lavg} for the last flapping cycle. C_L, C_D and C_m data history was then imported to MATLAB, while the Fluent data and case files were imported to Tecplot for data analysis.

CHAPTER 7

CFD PARAMETRIC STUDY

7.1 C_L-C_D Data Study

The entire data history was imported to MATLAB for every trajectory run and the plots for aerodynamic lift and drag coeficients C_L and C_D were obtained over the 51st cycle. Also, C_L values were averaged and plotted over each cycle to study the convergence of C_L over a flapping cycle. The C_L-C_D plot can be observed in two halves; downstroke upto a 500th of a second and upstroke from there on.

1. Elliptical Flapping Trajectory

   Fig 7.1 shows the C_L-C_D plot over the 51st cycle of the elliptical trajectory run. It can be seen from the C_L plot, both the strokes produce net positive values. However, the maximum value is reached during the upstroke which suggests that the upstroke contributes largely to the C_{Lavg} value. C_D For the downstroke, the C_D has a peak in the postive region while the upstroke brings it down to the negative region. This can be interpreted as the upstroke being the contributer to the thrust. Fig 7.2 shows the convergence plot for C_{Lavg} values. There is a steep decline in the value for the first few cycles. The value picks up and again declines gradually to a lower value.

   For 51st cycle,

   $C_{Lavg} = 0.0011$; $C_{Davg} = 6.122e^{-4}$

2. Straight Line Flapping Trajectory

As seen in fig 7.3, the C_L plot during the downstroke has two peak values with left slightly smaller than the right. This is primarily because during the downstroke, the wing pitch increases from zero at the start to a certain value before decreasing again to zero. So there are two points at which the wing will have same pitch angle thereby giving the required peaks in C_L values. However, for the first peak, there is a downwash on the wing due to the increasing wing pitch which lowers the C_L value. As for the second peak, there is an upwash due to the decreasing pitch angle thereby giving a slightly larger value. Similarly it can be explained why one can see a larger peak in C_L value at the start of the upstroke. The C_D plot for this case follows a similar pattern as in the elliptical case, but giving a lesser value. Fig 7.4 shows the C_{Lavg} converging to a slightly higher value than the elliptical case.

For 51st cycle,

$C_{Lavg} = 0.0012$; $C_{Davg} = 1.492e^{-4}$

3. Figure-8 Flapping Trajectory

   Fig 7.5 shows the C_L-C_D for the Figure-8 flapping trajectory. The C_L plot shows a sinusoidal beahvior for both the strokes, with the values fluctuating between the negative and positive region. The C_D values increases at the start of downstroke before decreasing to a negative value. The plot behaves in the exact inverse way for the upstroke, in all giving a net negative C_D. Fig7.6 shows the C_{Lavg} value decreasing steeply for the first 5 cycles before declining very gradually to a lower value.

   For 51st cycle,

   $C_{Lavg} = 0.0003941$; $C_{Davg} = -1.126e^{-5}$

4. Flapping Trajectory from Ueno et al. [2]

   As seen from fig 7.7, the C_L plot also has a sinusoidal behavior, but since the left lobe is bigger than the right lobe, C_L value is higher in the first peak than in the second peak. Similarly, in the C_D plot, there is a pronounced curve for the downstroke than in the upstroke. It can be seen from fig 7.8 that the C_{Lavg} convergence plot beahves the same way as in the Figure-8 trajectory.

   For 51st cycle,

   $C_{Lavg} = 0.0006356$; $C_{Davg} = -1.625e^{-4}$

7.2 Contour Plot Study

Fluent data and case files were imported to tecplot and contour plots for all the trajectory runs were studied. It was found that the results for all the cases could be best explained using the velocity vector plots. Figures 7.9 to 7.12 show the velocity vector plots for each trajectory. It can be seen from the figures that there are two counter-rotating vortices set up in the flow. The red solid circle in the figures shows the origin of the vortex while the curved arrows show the direction of vortex rotaton.

These vortices might be a result of wing flapping for a period of 51 cycles. Since the wing is flapping continuously in a bounded region, the air around it is nearly stagnant. The wing motion creates a vortex pattern in the flow. The viscous effects in the flow are not high enough to dampen the vortices. Furthermore, the low inlet air velocity of $0.01m/s$ is not able to push the vortices away from the wing. The building up of the vortices could be the reason of the declining values of C_{Lavg} for each trajectory. The vortex strength kept on increasing with each flapping cycle thereby reducing the C_{Lavg} value for each cycle.

However, the locations of vortices for each trajectory is different. This explains the different lift coefficient values for every trajectory. It can be seen from fig 7.11

and fig 7.12 that the vortex locations in these cases are above the wing location, while fig 7.10 shows that both the vortices are located below the wing location. As noted in the previous section, the straight path gives the maximum C_{Lavg} value and the Figure-8 path gives the minimum value.

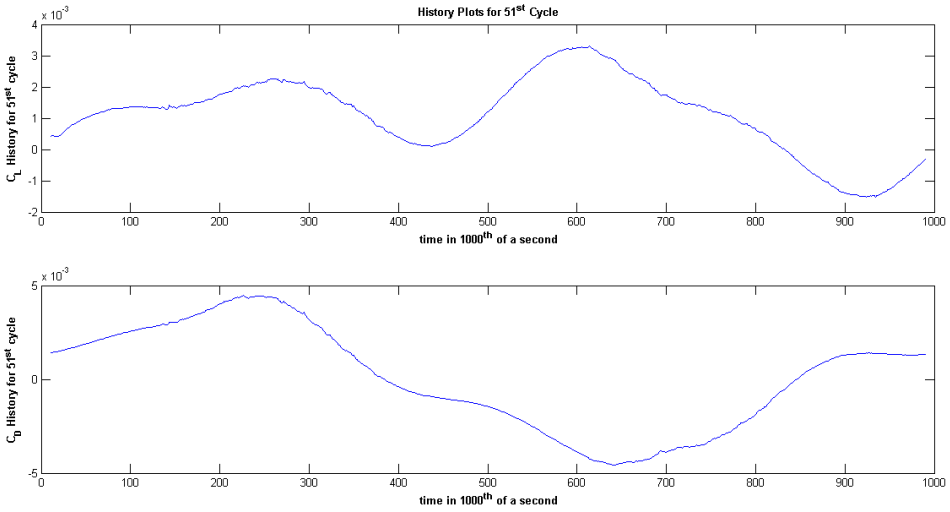

Figure 7.1. Aerodynamic coefficients plot for 51st cycle of elliptical trajectory.

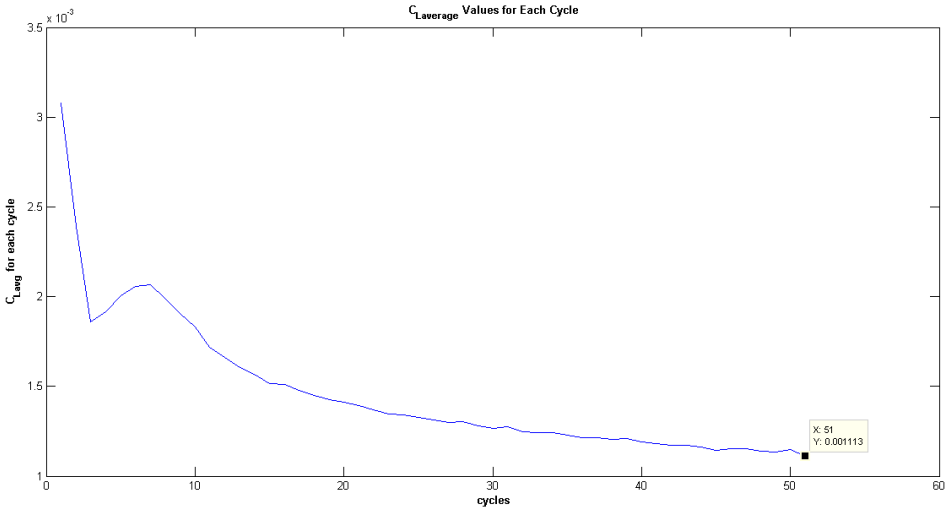

Figure 7.2. C_{Lavg} convergence plot for elliptical trajectory.

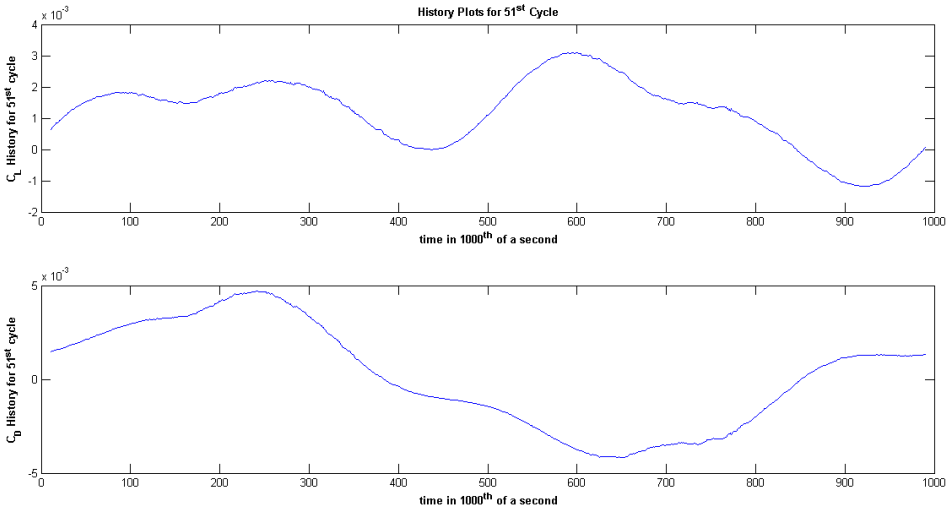

Figure 7.3. Aerodynamic coefficients plot for 51st cycle of straight line trajectory.

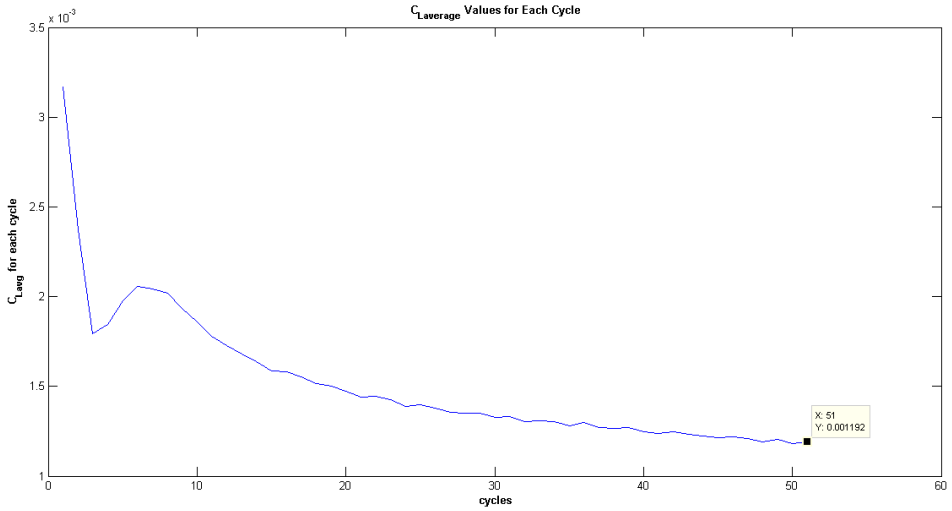

Figure 7.4. C_{Lavg} convergence plot for straight line trajectory.

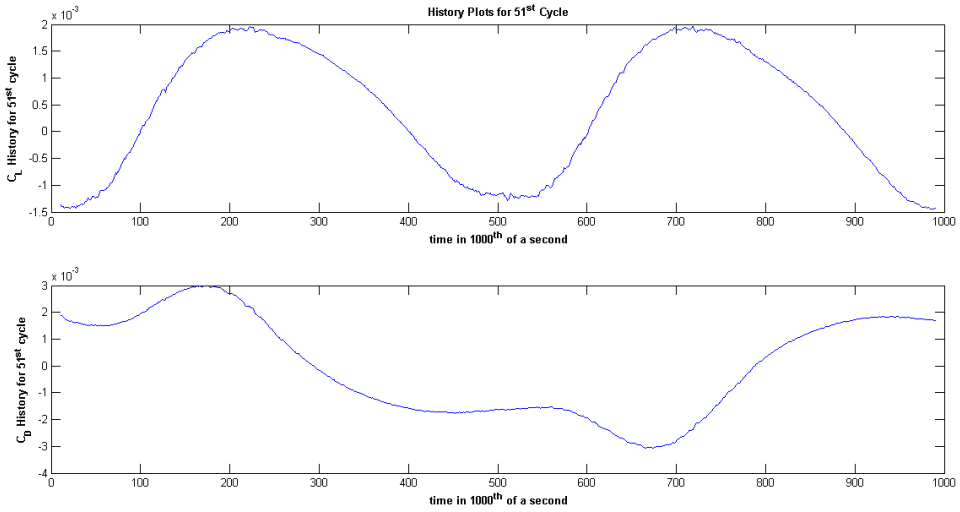

Figure 7.5. Aerodynamic coefficients plot for 51st cycle of Figure-8 trajectory.

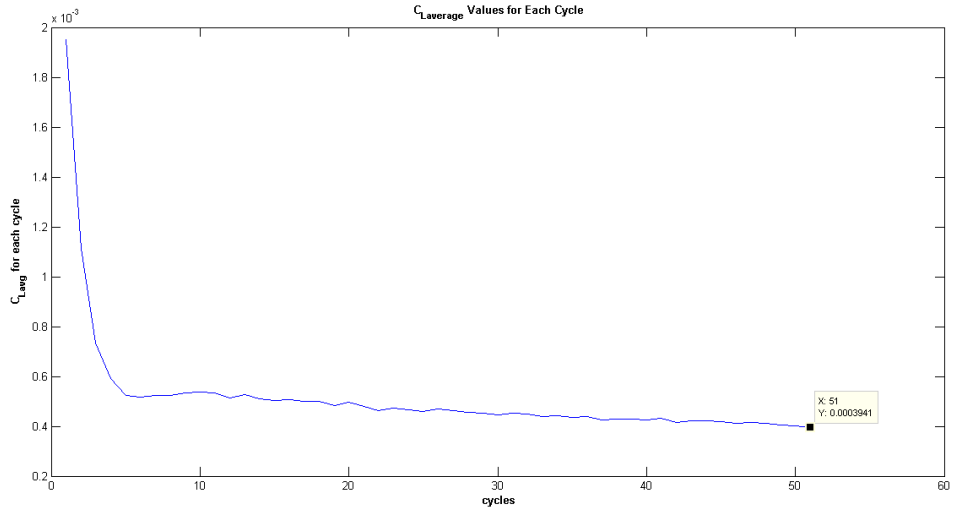

Figure 7.6. C_{Lavg} plot for Figure-8 trajectory.

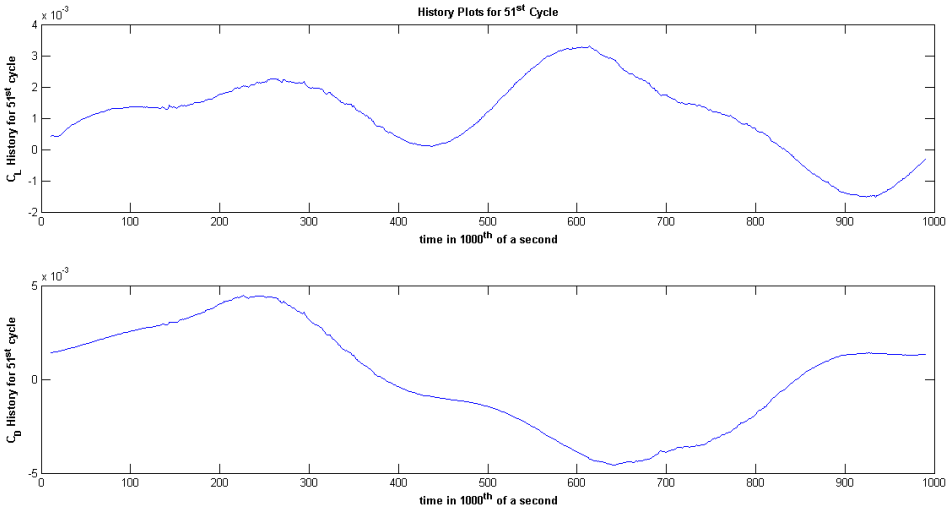

Figure 7.7. Aerodynamic coefficients plot for 51st cycle of flapping trajectory from Ueno et al. [2].

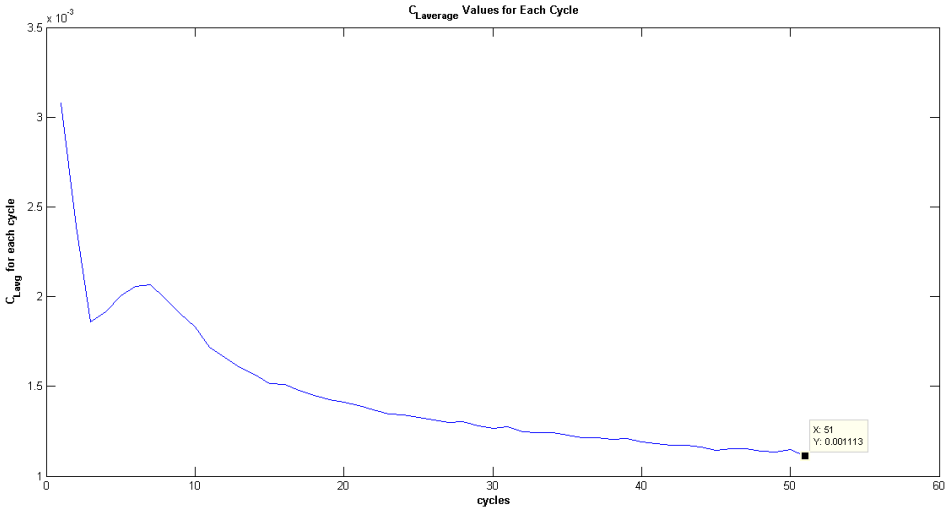

Figure 7.8. C_{Lavg} plot for flapping trajectory from Ueno et al. [2].

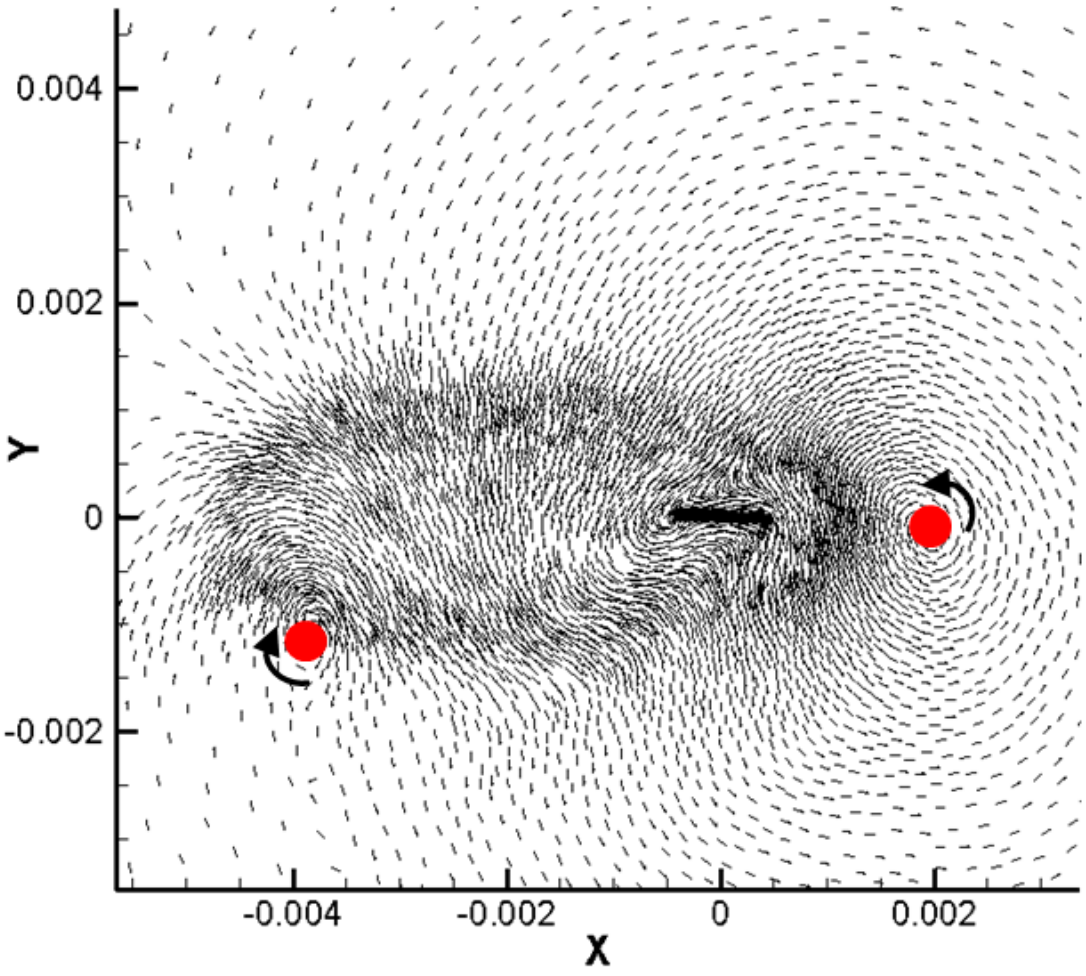

Figure 7.9. Velocity vector plot for elliptical trajectory.

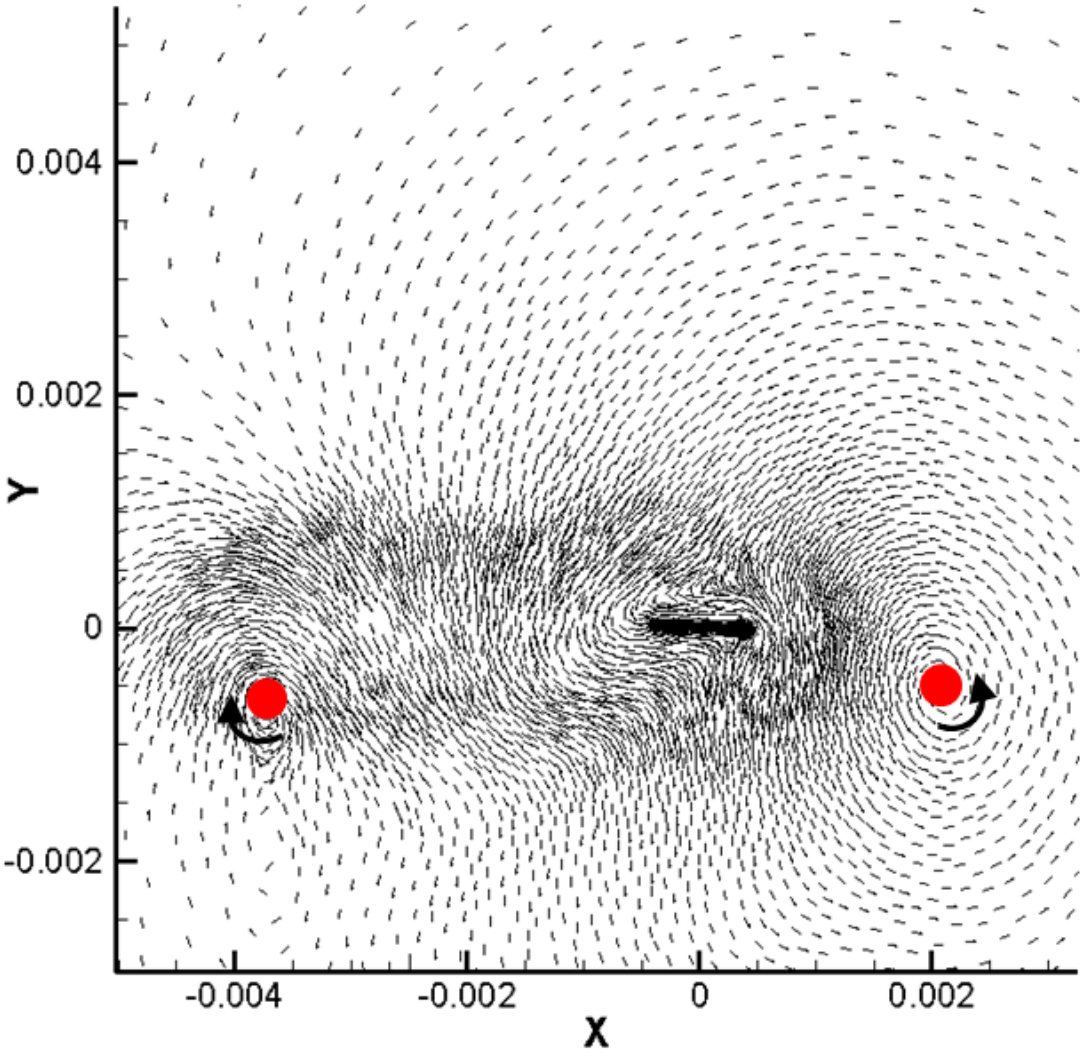

Figure 7.10. Velocity vector plot for straight line trajectory.

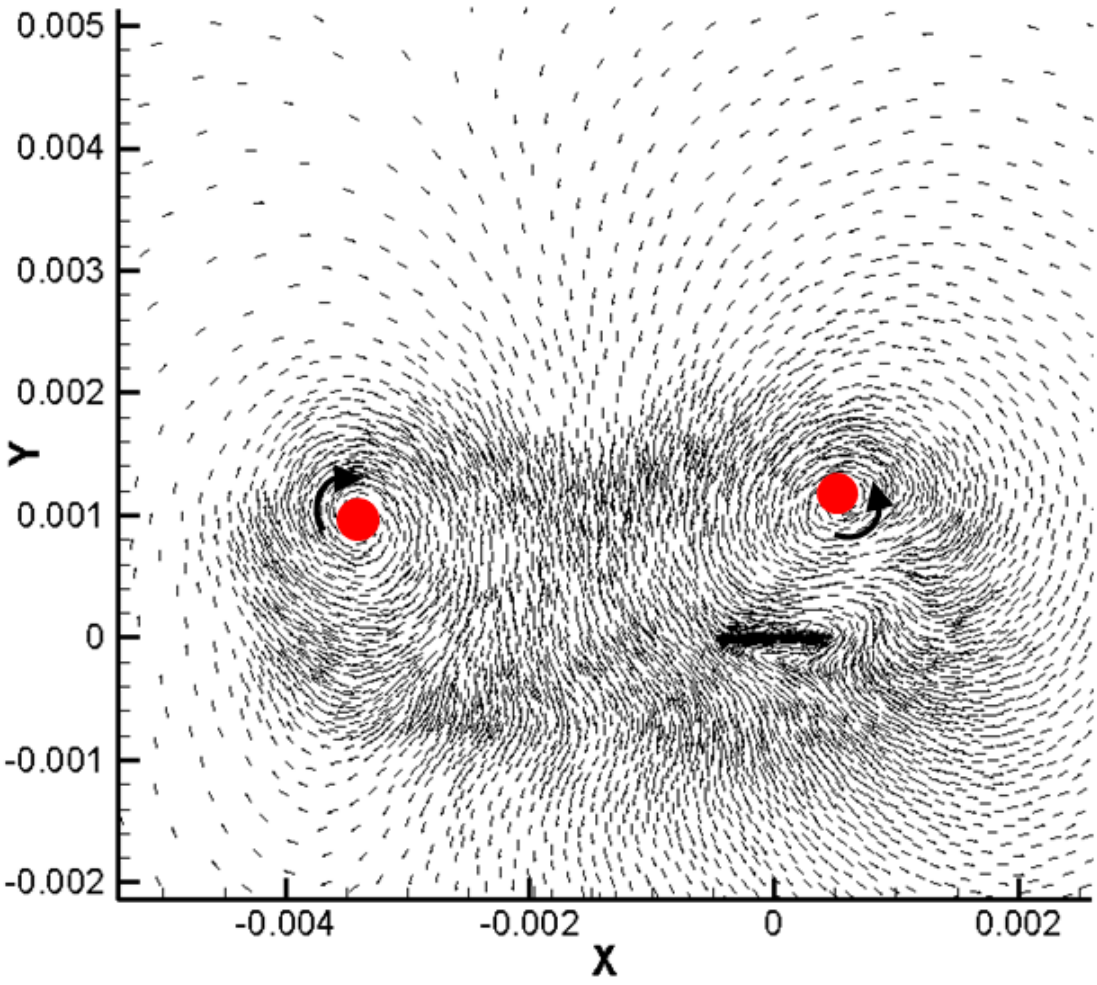

Figure 7.11. Velocity vector plot for Figure-8 trajectory.

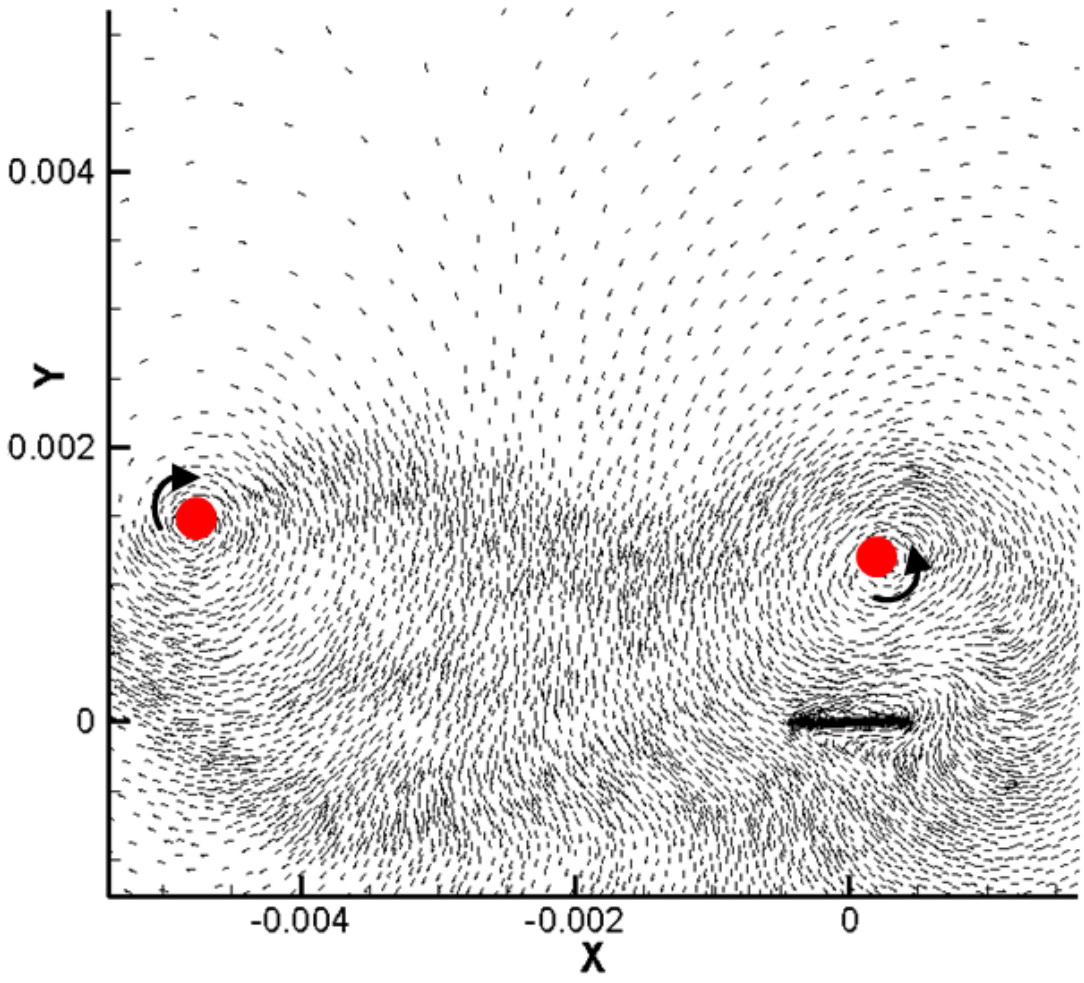

Figure 7.12. Velocity vector plot for flapping trajectory from Ueno et al. [2].

CHAPTER 8

CONCLUDING REMARKS

8.1 Summary

This research work presented the development of a nonlinear dynamic model that would give an accurate representation of the aerodynamic forces and moments acting on a flapping wing micro air vehicle for its complete flight dynamics study. The research was carried out in two segments:

- Nonlinear Dynamic Modeling and Simulation
- CFD based Parametric Study for Aerodynamic Model Development

The first segment started with a creation of a design model of the flapping wing MAV to be used for the study. MAV design model was based on Drosophila Melanogaster, an insect commonly known as fruit-fly. The model consisted of three rigid bodies; a main body and two wings with appropriate measurements. Different frames of reference were defined for the MAV and the equations of motion were derived using the first principles. The next step involved open loop simulation of the nonlinear dynamics using the aerodynamic model adopted from the open literature. The study of the simulation results showed inconsistencies in the boundedness of some parameters and effectuated the need for a new aerodynamic model.

The second part involved a CFD based parametric study of different flapping trajectories made by 2-D wing section of MAV to determine the variables required for the new aerodynamic model. A computational grid was created over a 2-D wing section. Four trajectories were generated using parametric functions. Unsteady incompressible Navier-Stokes equations were solved on an unstructured dynamic mesh

for different trajectories using CFD solver with user defined functions. Experiments were run for 51 cycles of flap and the data was post-processed for the parametric study. The study showed that for all the flapping trajectories, the values of average lift coefficient C_{Lavg} started at a higher value at the begining of the flap but gradually converged to a lower value as the number of cycles increased. It was seen from the velocity vector plots that this behavior was due to the presence of two counter-rotating vortices set up in the flow field due to continuous flapping. The location of this vortex pattern differed for each trajectory and so did the C_{Lavg} values.

A thorough sensitivity analysis needs to be performed vis-a-vis the parameters such as flow velocity, flapping frequency and mesh outer boundary to further investigate the development of flow field and its effects on the production of aerodynamic forces. This will help a great deal in determining the required variables for the new aerodynamic model.

8.2 Future Work

8.2.1 Nonlinear Dynamics with multi-body constraints

Mass and inertial effects of wings of the flapping wing MAV were neglected while deriving the nonlinear dynamics for simulations. This was a justifiable approximation since the wings contribute to only 3% of the total mass of the MAV. However it would be very interesting to observe if there is any change in the dynamic behavior of the MAV if these effects are included. The step in this direction would be to derive the nonlinear dynamics for this this multi-body constraint problem.

8.2.2 Determination of Variables for New Aerodynamic Model

As mentioned in section 8.1, the immediate goal is to study the effects of different parameters on the development of flow field around the flapping wings of the

MAV. This would be beneficial in coming up with a set of variables for the new aerodynamic model. Also, computational analysis of 3-D wing flapping motion would be looked into and steps to specify a correction factor for the 2-D case would be performed.

REFERENCES

[1] M. W. Oppenheimer, D. B. Doman, and D. O. Sigthorsson, "Dynamics and Control of a Biomimetic Vehicle Using Biased Wingbeat Forcing Functions," *Journal of Guidance, Control, and Dynamics*, vol. 34, no. 1, pp. 204–217, Jan. 2011.

[2] A. Ueno and B. H. Dennis, "Optimization of Flapping Airfoil Motion with Computational Fluid Dynamics," *International Review of Aerospace Engineering (I.RE.AS.E)*, vol. 2, no. April, pp. 104–111, 2009.

[3] F.-O. Lehmann and S. Pick, "The aerodynamic benefit of wing-wing interaction depends on stroke trajectory in flapping insect wings." *The Journal of experimental biology*, vol. 210, no. Pt 8, pp. 1362–77, Apr. 2007.

[4] T. Weis-Fogh, "Quick estimates of flight fitness in hovering animals, including novel mechanisms for lift production," *Journal of Experimental Biology*, vol. 59, no. 1, pp. 169–230, 1973.

[5] C. P. Ellington, "The Aerodynamics of Hovering Insect Flight. I. The Quasi-Steady Analysis," *Philosophical Transactions of the Royal Society B Biological Sciences*, vol. 305, no. 1122, pp. 1–15, 1984.

[6] ——, "The Aerodynamics of Hovering Insect Flight. II. Morphological Parameters," *Philosophical Transactions of the Royal Society B Biological Sciences*, vol. 305, no. 1122, pp. 17–40, 1984.

[7] ——, "The Aerodynamics of Hovering Insect Flight. III. Kinematics," *Philosophical Transactions of the Royal Society B Biological*

Sciences, vol. 305, no. 1122, pp. 41–78, 1984. [Online]. Available: http://rstb.royalsocietypublishing.org/cgi/doi/10.1098/rstb.1984.0051

[8] ——, "The Aerodynamics of Hovering Insect Flight. IV. Aeorodynamic Mechanisms," *Philosophical Transactions of the Royal Society of London Series B Biological Sciences 19341990*, vol. 305, no. 1122, pp. 79–113, 1984.

[9] ——, "The aerodynamics of hovering insect flight. V. A vortex theory," *Philosophical Transactions of the Royal Society of London Series B Biological Sciences*, vol. 305, no. 1122, pp. 115–144, 1984.

[10] ——, "The Aerodynamics of Hovering Insect Flight. VI. Lift and Power Requirements," *Philosophical Transactions of the Royal Society of London Series B Biological Sciences 19341990*, vol. 305, no. 1122, pp. 145–181, 1984.

[11] J. M. Zanker, "The Wing Beat of Drosophila Melanogaster. I. Kinematics," *Philosophical Transactions of the Royal Society B: Biological Sciences*, vol. 327, no. 1238, pp. 1–18, Feb. 1990.

[12] J. M. Zanker and K. G. Gotz, "The Wing Beat of Drosophila Melanogaster. II. Dynamics," *Philosophical Transactions of the Royal Society B: Biological Sciences*, vol. 327, no. 1238, pp. 19–44, Feb. 1990.

[13] G. K. Taylor and A. L. R. Thomas, "Dynamic flight stability in the desert locust Schistocerca gregaria," *Journal of Experimental Biology*, vol. 206, no. 16, pp. 2803–2829, 2003.

[14] B. Etkin, *Dynamics of Atmospheric Flight*. New York: Wiley, 1972.

[15] M. Sun and Y. Xiong, "Dynamic flight stability of a hovering bumblebee." *Journal of Experimental Biology*, vol. 208, no. Pt 3, pp. 447–459, 2005.

[16] T. R. K. Dudley and C. P. Ellington, "Mechanics of forward flight in bumblebees. II. quasi-steady lift and power requirements," *Journal of Experimental Biology*, vol. 148, pp. 53–88, 1990.

[17] D. B. Doman, M. W. Oppenheimer, and D. O. Sigthorsson, "Dynamics and Control of a Minimally Actuated Biomimetic Vehicle : Part I - Aerodynamic Model," *AIAA Guidance Navigation and Control Conference*, vol. AIAA 2009-, no. August, pp. 1–25, 2009.

[18] D. B. Doman and D. O. Sigthorsson, "Dynamics and Control of a Minimally Actuated Biomimetic Vehicle : Part II - Control," in *AIAA GNC 2009*, no. August, 2009, pp. 1–23.

[19] R. J. Wood, "The First Takeoff of a Biologically Inspired At-Scale Robotic Insect," pp. 341–347, 2008.

[20] S. P. Sane and M. H. Dickinson, "The control of flight force by a flapping wing: lift and drag production." *The Journal of experimental biology*, vol. 204, no. Pt 15, pp. 2607–26, Aug. 2001.

[21] M. Sun, J. Wang, and Y. Xiong, "Dynamic flight stability of hovering insects," *Acta Mechanica Sinica*, vol. 23, no. 3, pp. 231–246, May 2007.

[22] J. H. Wu, Y. L. Zhang, and M. Sun, "Hovering of model insects: simulation by coupling equations of motion with Navier-Stokes equations." *Journal of Experimental Biology*, vol. 212, no. Pt 20, pp. 3313–3329, 2009.

[23] G. Gebert, P. Gallmeier, and J. Evers, "Equations of motion for flapping flight," *AIAA Paper, AIAA*, vol. 4872, no. August, 2002.

[24] C. T. Orlowski and A. R. Girard, "Modeling and Simulation of Nonlinear Dynamics of Flapping Wing Micro Air Vehicles," *AIAA Journal*, vol. 49, no. 5, pp. 969–981, May 2011.

[25] W. Shyy, Y. Lian, J. Tang, H. Liu, P. Trizila, B. Stanford, L. Bernal, C. Cesnik, P. Friedmann, and P. Ifju, "Computational aerodynamics of low Reynolds number plunging, pitching and flexible wings for MAV applications," *Acta Mechanica Sinica*, vol. 24, no. 4, pp. 351–373, July 2008.

[26] M. Sun and D. Gang, "Lift and power requirements of hovering insect flight," *Acta Mechanica Sinica*, vol. 19, no. 5, 2003.

[27] Z. Jane Wang, "Two dimensional mechanism for insect hovering." *Physical review letters*, vol. 85, no. 10, pp. 2216–9, Sept. 2000.

[28] R. Ramamurti and W. C. Sandberg, "A three-dimensional computational study of the aerodynamic mechanisms of insect flight." *The Journal of experimental biology*, vol. 205, no. Pt 10, pp. 1507–18, May 2002.

[29] M. H. Dickinson, "Wing Rotation and the Aerodynamic Basis of Insect Flight," *Science*, vol. 284, no. 5422, pp. 1954–1960, June 1999.

[30] P. Bai, E. Cui, F. Li, W. Zhou, and B. Chen, "A new bionic MAVs flapping motion based on fruit fly hovering at low Reynolds number," *Acta Mechanica Sinica*, vol. 23, no. 5, pp. 485–493, Sept. 2007.

[31] A. Ennos, "The Kinematics an Daerodynamics of the Free Flight of some Diptera," *Journal of Experimental Biology*, vol. 142, no. 1, p. 49, 1989.

[32] A. Azuma, S. Azuma, I. Watanabe, and T. Furuta, "Flight mechanics of a dragonfly," *Journal of experimental biology*, vol. 116, no. 1, pp. 79–107, 1985.

[33] B. W. Tobalske, D. R. Warrick, C. J. Clark, D. R. Powers, T. L. Hedrick, G. a. Hyder, and A. a. Biewener, "Three-dimensional kinematics of hummingbird flight." *The Journal of experimental biology*, vol. 210, no. Pt 13, pp. 2368–82, July 2007.

[34] M. Sun and J. Tang, "Lift and power requirements of hovering flight in Drosophila virilis." *The Journal of experimental biology*, vol. 205, no. Pt 16, pp. 2413–27, Aug. 2002.

[35] ——, "Unsteady aerodynamic force generation by a model fruit fly wing in flapping motion." *The Journal of experimental biology*, vol. 205, no. Pt 1, pp. 55–70, Jan. 2002.

[36] M. A. Groen, "PIV and force measurements on the flapping-wing MAV DelFly II," Master's degree thesis, Delft University of Technolgy, 2010.

[37] H. Liu, "Integrated modeling of insect flight: From morphology, kinematics to aerodynamics," *Journal of Computational Physics*, vol. 228, no. 2, pp. 439–459, Feb. 2009.

[38] A. Azuma, *The biokinetics of flying and swimming.* American Institute of Aeronautics and Astronautics, Inc., 2006.

[39] Z. J. Wang, "Unsteady forces and flows in low Reynolds number hovering flight: two-dimensional computations vs robotic wing experiments," *Journal of Experimental Biology*, vol. 207, no. 3, pp. 449–460, Feb. 2004.

BIOGRAPHICAL STATEMENT

Alok A. Rege was born in the city of Mumbai, India in 1984. He obtained a Bachelor's degree in Aeronautical Engineering with a major in Aerodynamics from the Aeronautical Society of India (AeSI), New Delhi in 2009. After graduation he worked as a Research Intern in the 'Lighter Than Air Systems (LTA)' lab under Dr. Rajkumar Pant at the Indian Institute of Technology (IIT), Bombay. He then came to the United States in Fall 2010 to pursue an M.S. degree program in Aerospace Engineering at the University of Texas at Arlington.

Alok has been a Graduate Teching Assistant at UTA for the courses of Introduction to Automatic Control, Engineering Statics and Engineering Analysis. His research interests include flight dynamics & controls and computational fluid dynamics (CFD). He is currently working in the Aerospace Systems Lab (ASL) with Dr. Kamesh Subbarao and in the CFD Lab with Dr. Brian Dennis on the development of a Micro Air Vehicle. He is a graduate member of AeSI and a student member of AIAA.